Runaway electrons in tokamak disruptions in the presence of impurities

Luigino Capone

Department of Applied Physics

Chalmers University of Technology

A thesis submitted for the degree of

Applied Physics

February 21th 2013

Acknowledgements

I would not have been able to write this thesis without the support of many people and I would like to take the opportunity to thank some of them here. First of all, a big thank you to both my supervisors Prof.Tünde Fülöp and Gergely Papp who made my experience at Chalmers possible and patiently guided me in the right direction through suggestions and interesting discussions. I would like to thank my colleagues at the Nuclear Engineering Department, especially those of the Fusion Group for keeping their doors open and offering advice on small as well big issues.

A huge thank you to my parents, who offer great support with this study period abroad and have supported me all the way since the beginning of my studies and without whom I would have found it very difficult to achieve this goal. Last but not least, thanks to Mariagrazia, for always understanding when I have needed to work hard and for being supportive and enthusiastic of my stay in Sweden. Maybe a day will be my turn to return her the help she gave me.

Abstract

Disruptions in tokamak devices are phenomena where the plasma loses its confinement suddenly, on time scales of a few milliseconds, releasing most part of the plasma energy onto the machine components. These phenomena are dangerous to the plasma-facing components and they pose a severe threat to the machine's integrity, causing the deposition of intense thermal fluxes on the first wall materials and serious electromagnetic stresses on the structure. High-energy runaway electrons are also generated due to disruptive phenomena, causing further damage to the machine. The recent successful installation of the JET ITER-like wall (ILW) in place of the previous carbon-based wall, suggests an assessment of the impact of different wall composition on the runaway production. Extracting experimental data from two different plasma discharges equipped respectively with beryllium and carbon wall, the production of runaway electrons has been investigated through a numerical code. Simulations for the evolution of runaway electrons have been carried out for different scenarios, considering both a prescribed exponential temperature decay and disruptions triggered by an argon injection scenario. Argon and carbon/beryllium impurities coming from the sputtering of the first wall has also been included in a further scenario. A comparison of two different discharges in terms of generation mechanisms for runaways has also been performed, together with various scans for different argon concentrations. Simulations showed that impurities coming from different walls, have a different impact on the produced runaway currents and on generation mechanisms.

Contents

List of Figures

Notation

Acronyms / Abbreviations

- $\langle \sigma v \rangle$ Average cross section

- λ_D Debye length

- : dot product for matrices

- D_{RR} Rechester-Rosenbluth coefficient

- k_b Boltzmann's constant ($1.3806488 \cdot 10^{-23} J K^{-1}$)

- **ETB** Edge Transport Barrier

- **FW** First Wall

- **ILW** ITER-like wall

- **ITB** Internal Transport Barrier

- **NBI** Neutral Beam Injection

- **PFC** Plasma Facing Components

- **RE** Runaway Electron

Chapter 1

Energy scenarios

1.1 The need for energy

The amount of available energy is one of the fundamental pillars of all civilizations, and it is undeniably closely related to the development and wealth of nations. In general, future scenarios for energy are very difficult to forecast but at the same time they are essential tools for policymakers. Furthermore, even if such scenarios are inevitably influenced by current views and expectations, some trends are regarded as unavoidable for the future of energy.

One of the most impacting factors dictating the future energy scenarios is population growth. World population will grow from 6 billion people in 1999 to about 8 billion in 2025, ending up at some 9-10 billion people in 2050, according to United Nation estimates [6]. Together with the economic growth, the emergence of massive new energy demands in countries like China and India and the concentration of oil and natural gas suppliers, the shift to higher energy prices worldwide is going to become a real global challenge. In addition, it seems there is no possibility to sustain the current growth rates in the future (Fig.1.1) both from energetic and environmental perspective, therefore changes in the structure of the current world energy strategy are inevitable.

Sustainability in the current overall energy strategy is absent: limitations of the world's fossil fuel resources, especially oil and gas, and no new proven reserves
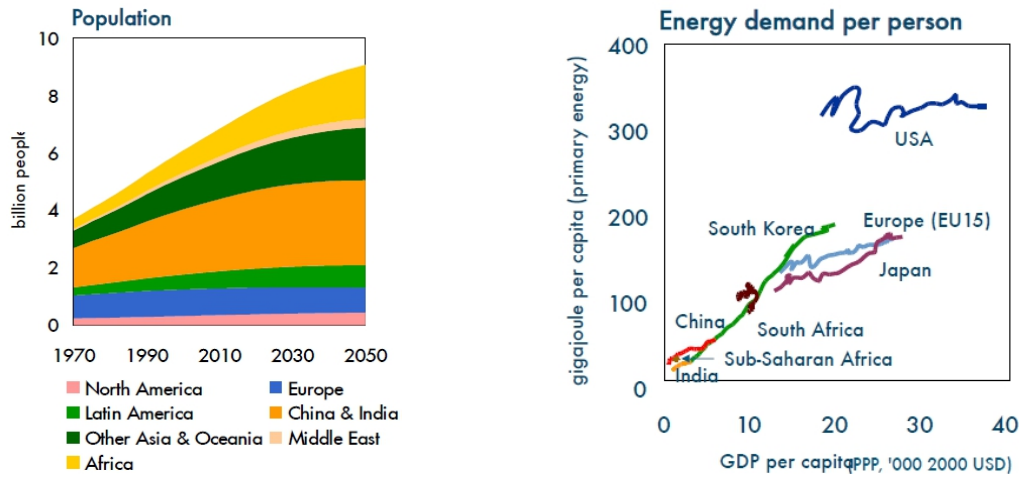
Figure 1.1: a) Population growth in world macro-areas, b)Energy demand as function of GDP per capita [1][2]

available depict a scenario where affordable energy coming from fossil sources is going to inevitably vanish during the 21st century (Fig.1.2). We also need to face the crucial challenges related to global warming and, in general, to the climate change that would limit the composition of the energetic mix and reduce the energy sources responsible for massive CO_2 production and pose further serious limits to the current energetic strategies.

1.2 Renewables and nuclear energy

Renewable energy sources are viewed by the policymakers and general public as a possible solution to the problems posed by the increasing energy demand(Fig.1.3). In fact, renewable sources, such as wind power, solar power and hydroelectric power show a number of advantages in terms of pollution and environmental sustainability. Nevertheless renewable sources of energy suffer limitations in geographical and time availability, compounded by the fact that the issue of energy storage has yet to be fully resolved.
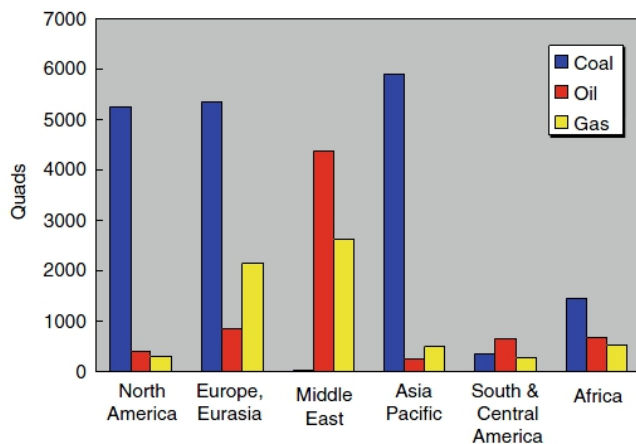
Figure 1.2: Proven fossil reserves of the world [3]

Wind energy, for example, is an excellent way to increase the available world electric power and to reduce[1] the impact on the environment, but wind is not a resource that is uniformly distributed over the globe, with many countries unable to rely on such an energy source alone. Wind is also barely predictable and essentially intermittent, and even if new technologies (e.g. smart grids) are currently under development to overcome this aspect, no convenient methods for energy storage are currently available. A primary energy source should be able to face both peak loads and steady energy demand. Wind energy can not guarantee this but rather would serve better as a precious auxiliary energy source.

Solar power has advantages and disadvantages similar to wind energy: the sun is not shining everywhere with the same intensity, solar energy is intermittent and difficult to store, and centralized solar plants are installations requiring considerable surfaces.

A necessary feature for a primary energy source is to be able to provide sufficient energy: the world energy consumption (Fig.1.3) and its increasing growth rates need for primary sources that are reliable, continuous and able to satisfy a

---

[1]It is important to stress that even renewable energy sources have a *fossil footprint*, that includes all the consumption of fossil resources from the mining phase (e.g. silicon for solar cells) to the equipment manufacturing, including transportation of raw materials and the maintenance of the equipment itself.
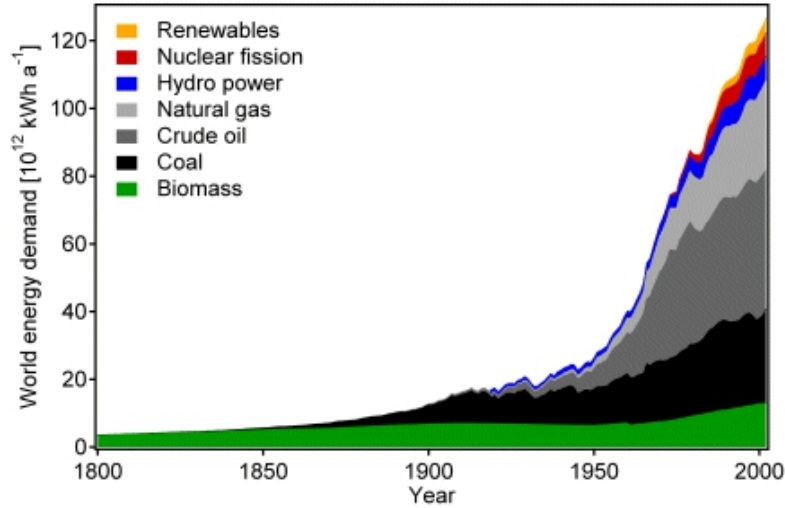
Figure 1.3: World energy consumption (in 10^{12} kWh/year units) [4]

significant share of the whole energy demand.

Nuclear (fission) energy is a well-known technology, provides continuous and large energy amounts and it does not produce CO_2 or other greenhouse gases. On the other hand, danger of accidents, proliferation and still unanswered questions regarding waste storage remain, making its further growth difficult.

Moreover, uranium is not renewable and recent studies [7] claimed that the known reserves will expire in several decades at the current consumption rates. However, including conventional and unconventional sources and recycling of nuclear fuel, the same research pointed out that even at generation rates ten times greater than current levels, there are sufficient resources for many centuries of energy production, and technology developments would greatly extend these period.

Summing up the future energy scenarios, one should consider oil shortage as the most imminent issue, but all the fossil fuels are doomed to be depleted in the short-medium period and also contributing significantly to global environmental issues. Considering also the current growth of many countries, energy problems require a portfolio of options and the development of fusion can play an increasing role because it would be a big step in creating energy abundance while

4

avoiding drawbacks, such as shortage of fuel and long-term radioactive wastes, and providing a primary backbone energy source at a reasonable price. Additional advantages to utilizing nuclear fusion include no CO_2 emission and no increased proliferation risks. Furthermore, encouraging estimates have been carried out about its beneficial economic influence [8] [9]. The real challenge in the upcoming years will be to overcome the scientific and engineering problems involved in the design of a controlled fusion device.

Chapter 2

Confined plasma physics

2.1 Nuclear fusion

2.1.1 Nuclear reactions and plasmas

While the energy in nuclear fission comes from the energy released by the splitting of heavy nuclei, nuclear fusion processes release energy when two light nuclei fuse together to form a heavier nucleus.

According to Einstein's energy-mass equivalence principle, as the mass of the resulting nucleus is lower then the mass of the two reacting nuclei, the missing quantity (known as *mass defect*) is converted into energy during the fusion process. Typical nuclear reactions leading to fusion and the production of considerable amounts of energy involve the hydrogen isotopes deuterium (^{2}H) and tritium (^{3}H):

$$^2\text{H} + {}^2\text{H} = {}^3\text{H} + {}^1\text{H} + 4.03 MeV$$

$$^2\text{H} + {}^2\text{H} = {}^3\text{He} + n + 3.27 MeV$$

$$^2\text{H} + {}^3\text{He} = {}^4\text{He} + {}^1\text{H} + 18.3 MeV$$

$$^2\text{H} + {}^3\text{H} = {}^4\text{He} + n + 17.59 MeV$$
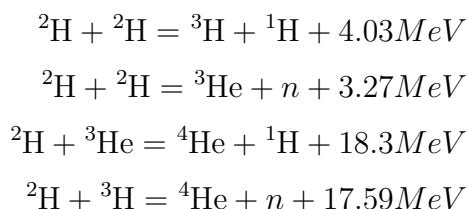
To obtain a fusion reaction, it is necessary that the two nuclei get sufficiently close together to make the nuclear strong force overwhelm the electrostatic repul-

sion due to their electric charge. The electrostatic barrier becomes (classically) surmountable at distances on the order of the femtometer (10^{-15} meters).

The simplest way to reach such distances between particles is to raise the temperature, thus increasing the kinetic energy of the particles. The probability that two sufficiently energetic nuclei fuse together depends both on the densities of the atomic species i, j and the (average) cross section $\langle \sigma v \rangle$ of the mixture. The probability of reaction per unit time per unit density probability is proportional to the *reactivity* parameter R:

$$R = \prod_{i,j} n_i n_j \langle \sigma v \rangle . \tag{2.1}$$

The peak of the reactivity, for the most common reactions just presented, occurs at different values of temperature and this makes the most promising reaction to be the deuterium-tritium one, as the ^{2}H-^{3}H reaction reaches its maximum reactivity at a (relatively) modest temperature, around 64 keV.
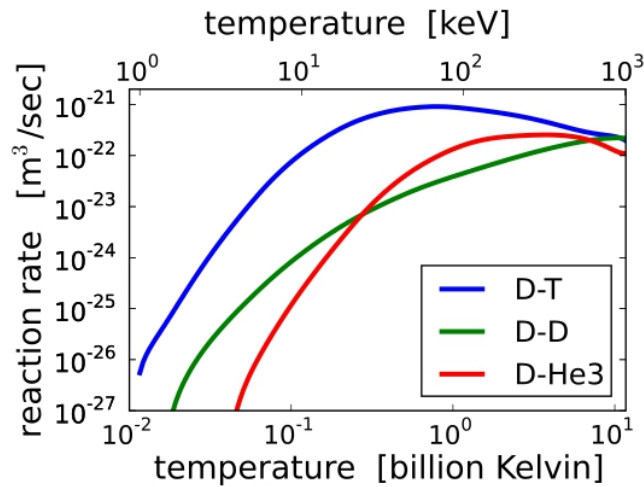
Figure 2.1: Reactivity as a function of temperature and reaction

When it comes to the fuel supply, one has to recognise that deuterium occurs naturally in water. It is widespread and abundant in nature and represents an ideal candidate as fuel for nuclear fusion. Tritium, on the other hand, is present in nature only in traces. It is radioactive and it can be produced through neutron

activation of lithium-6 [10] :

$$n + {}^6\text{Li} = {}^4\text{He}(2.05MeV) + {}^3\text{H}(2.75MeV). \tag{2.2}$$
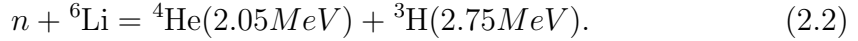
For a fusion reactor to operate in steady state, the fusion plasma must be maintained at a constant temperature, therefore the optimal conditions for energy and density are to be held (adding energy at the same rate the plasma loses energy) for the characteristic time of decrease in plasma energy (called the *confinement time* τ_{conf}) in order to keep the *triple product* $n\tau_{conf}T$ over the threshold that allows net energy production [11].

At the temperatures needed for achieving fusion conditions, matter is in a plasma *state*, in which an important fraction of the atoms is completely ionized, so that electrons and ions are separated.

Plasmas resulting from ionization of neutral gases contain the same number of electrons and ions. The oppositely charged particles are strongly coupled and tend to electrically neutralize one another on macroscopic length-scales, showing a *quasi-neutral* behavior:

$$n_e \approx n_i \equiv n. \tag{2.3}$$

For such a system made up of electrons and ions, respectively with mass m_e and m_i, a *kinetic temperature* T can be defined, for the species s , as:

$$T_s = \frac{1}{3k_B} m_s \langle v_s^2 \rangle, \tag{2.4}$$

where $\langle v_s^2 \rangle$ is an average over the velocity distribution. The most fundamental time-scale in a plasma is given by the *plasma frequency* (different for each species s),

$$\omega_s^2 = \frac{ne^2}{\epsilon m_s}, \tag{2.5}$$

corresponding to the electrostatic oscillation frequency in response to a small perturbation of the charge distribution. This means that plasmas shield electric potentials in the sense that if an electromagnetic disturbance enters a plasma, the plasma tends to shield out the field. The shielding length is called the *Debye*

length λ_D and characterizes the degree of interaction (or *coupling*) of the plasma:

$$\lambda_D = \sqrt{\frac{\varepsilon k_B T}{n_e e^2}}, \tag{2.6}$$

where k_B is the *Boltzmann constant*, n_e is the plasma density, T is the kinetic temperature and ε represents the electric permittivity.

Extracting energy from this nuclear process still remains a central question: there is no material which can endure temperatures on the order of several million degrees for a sufficient amount of time to allow for an effective confinement.

2.1.2 Fields and confinement

The most promising way to solve the confinement problem for plasmas is magnetic confinement. Moving from an idea coming from the Soviet physicist Sacharov, the development of a toroidal chamber in which the plasma would be confined thanks to the use of toroidal and poloidal[1] magnetic fields (Fig.2.2,2.3), lead to the modern *tokamak* architectures [12].

As the plasma is made of charged particles, with magnetic fields one can confine it using closed magnetic surfaces. The equation governing the motion of the *j*-th charged particle in an electromagnetic field has the form:

$$m_j \frac{d\mathbf{v}_j}{dt} = q_j \mathbf{v}_j \times \mathbf{B}, \tag{2.7}$$

hence the motion of the particle becomes helical along the toroidal magnetic field line. The radius of this helical motion (the *gyro radius* or *Larmor radius*) and the frequency (*cyclotron frequency*) are expressed as:

$$\rho_j = \frac{m_j v_0}{q_j B} \tag{2.8}$$

$$\omega_j = \frac{q_j B}{m_j} \tag{2.9}$$

---

[1]The toroidal angle ϕ is in the horizontal plane of the torus, while the poloidal angle θ describes the rotation in a cross-section of the torus. R and r are, respectively, the major and minor radii.
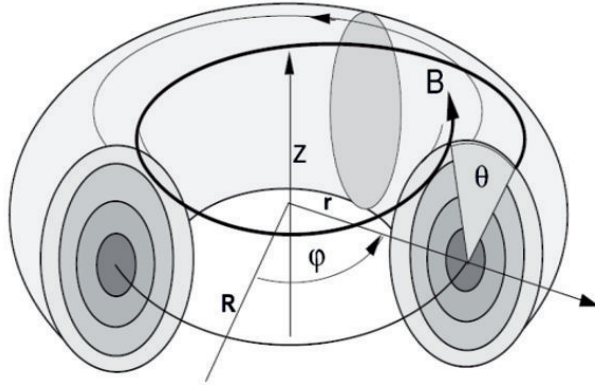
Figure 2.2: Toroidal Geometry.

Adopting a toroidal geometry solves the problems related to end losses but it presents drift effects coming from the geometrical nature of the torus.

As magnetic field lines are curved, charged particles moving along them are subject to a vertical drift caused by the inhomogeneity and the curvature of the magnetic field. Ions and electrons drift vertically in different directions because of the different charge, creating a charge separation and an associated electric field. Due to this, a drift motion occurs in the radially outward direction

$$v_E = \frac{E \times B_\phi}{B_\phi^2}.$$ (2.10)

This drift will move the plasma to the wall in a short time unless a poloidal magnetic field is applied preventing charge separation (and radial drift) formed in a pure toroidal field. Helical field lines therefore connect the upper and lower part of the tokamak, generating the characteristic twisted magnetic field line along the torus.

2.1.3 Tokamak devices

From the very beginning of the tokamak era, controlled nuclear fusion research faced huge scientific and technical challenges. The increasing impact of costs and
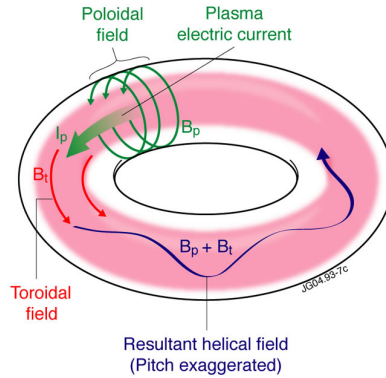
Figure 2.3: Toroidal and poloidal magnetic fields

the fundamental role of sharing knowledge among the scientific community, even supported by political will, initiated an era of international collaboration.

The *Joint European Torus (JET)*, located in Culham (UK), was the first controlled fusion device built through a joint European effort. Since 1983, when the first plasma was created, its contribution to the study of the scientific feasibility of nuclear fusion control has been fundamental and has led to major advances in the science and engineering of fusion [13].

It remains still the largest and most powerful tokamak ever built, and is the only device currently capable of using the deuterium-tritium fuel mix, and is devoted to demonstrating the feasibility of magnetic fusion reactor physics.

The roadmap towards the realization of a working fusion reactor requires further steps to optimize physics scenarios already tested in JET and net energy production [14].

ITER is destined to be the natural successor of JET, focusing on technological aspects needed in the perspective of a fusion-based electric power plant. In particular, ITER is a large-scale scientific experiment funded by the European Union, India, Japan, China, Russia, South Korea and the United States, aimed at proving the feasibility of fusion power through a full exploration of the relevant science and key technological components for future fusion power plants [15]. Concurrently, advanced fusion materials research will contribute to characterize

new materials essential for the successful operation of a fusion power plant. In this perspective, the *International Fusion Materials Irradiation Facility* (*IFMIF*) will be developed as a joint project between the EU and Japan. This facility will be able to test advanced fusion materials under neutron fluxes similar to those expeted inside a fusion reactor [16].

Assuming ITER's success, it remains a gap between ITER and a commercial power plant (Fig.2.4) because of the larger dimension requested to the latter. The information, technologies and experience provided by ITER will be crucial to the development of a demonstration power plant (*DEMO*).
DEMO will generate significant amounts of electricity, up to 500 megawatts, over extended periods and will integrate and demonstrate all relevant technologies in a prototype fusion power plant. It will be also the last research machine before a commercial fusion power plant (FPP) [17][18].
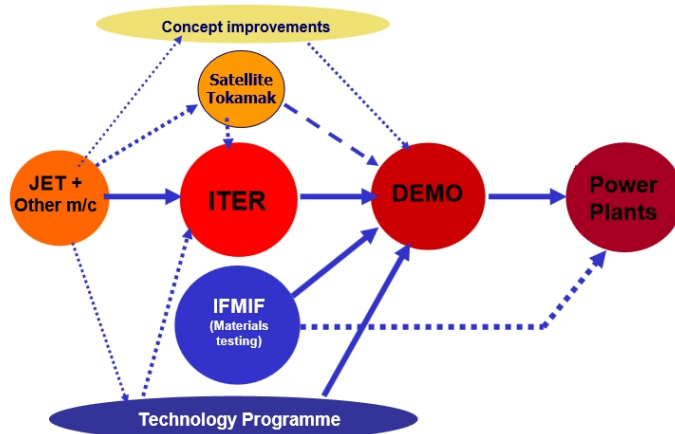
Figure 2.4: A roadmap to fusion power: roles of ITER and DEMO

2.2 Kinetic models

Plasmas are made up of a large number of particles. Taking into account trajectories and mutual interactions among a large number of charged particles under the influence of an external electromagnetic field would be a computationally expensive task. Moreover, such an approach would be in many cases unnecessary,

as the main aim is to model macroscopic behaviour rather than single particle evolution. These issues are highly analogous to those encountered for gases. Thus an approach based on statistical mechanics and kinetic theory can also be helpful in plasmas.

2.2.1 Collision models

A realistic model for a fusion plasma needs to include the effects of mutual electromagnetic interactions among the plasma particles, namely *collisions*. A collision changes the particle's velocity modulus and direction. Mathematically it is modeled through the use of the *distribution function* $\mathbf{f}(\mathbf{r}, \boldsymbol{v}, t)$ and the *collision operator* on the right-hand side of the *Vlasov-Poisson equation*[19]:

$$\frac{\partial \mathbf{f}}{\partial t} + \mathbf{v} \cdot \nabla \mathbf{f} + \frac{q_\alpha}{m}(\mathbf{E} + v \times \mathbf{B}) \cdot \nabla_v \mathbf{f} = \frac{\partial \mathbf{f}}{\partial t}\bigg|_C. \tag{2.11}$$

The collisional Vlasov-Poisson equation (2.11) is generally recognized under the name of the *Vlasov-Poisson-Fokker-Planck equation* (VPFP for short) and the collisional term $\mathcal{C}(\mathbf{f}) = \frac{\partial f}{\partial t}\big|_C$ is known as the *Fokker-Planck operator*.

The use of the term "collision" implies a sort of mechanical interaction among particles in the highly ionised plasma fluctuating in a tokamak vacuum vessel. This is, however, definitely not the case because the particles are charged and will "feel" each others' fields long before they can make contact with each other.

In fact, Coulomb interactions are to be seen as a deflection of an incoming charged particle due to the electric field of another particle to which the former one passes sufficiently close.

What "sufficiently close" means, from a quantitative point of view, depends on the Debye length λ_D. Fixing an impact parameter b expressing the distance at which the particles pass each other, the "projectile" particle can feel the field of the "target" particle only if b is smaller than the radius λ_D of the spherical region in which the Debye shielding effects are measurable. Outside the sphere, the shielding effects dominate and no Coulomb interactions are present.
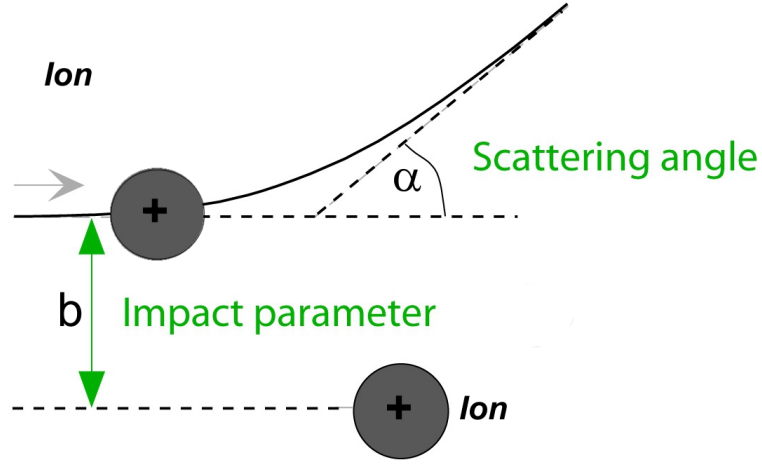
Figure 2.5: Coulomb collision scheme

Inside the Debye sphere, the interaction between charges can be modeled as an electrostatic force F_E:

$$F_E = \frac{q_i q_j}{4\pi\epsilon_0 r^2(t)}, \tag{2.12}$$

where q_i and q_j are the charges of the ion and electron respectively, $r(t)$ is the distance between the centres of the two particles, and ϵ_0 is the electric permittivity.

Electrons are scattered by the Coulomb field of the ions and here it is assumed that ions move much more slowly as their masses are much greater than those of the electrons, hence they can be treated as if at rest.

If the deflection $\alpha \ll 1$ is small, the model can be simplified, approximating the angle by computing the perpendicular impulse exerted by the Coulomb field on the ion and then integrating along the unperturbed straight line trajectory:

$$m_e \Delta v_y \alpha = \int_{-\infty}^{+\infty} \frac{e^2 b}{4\pi\epsilon_0(b^2 + v_e^2 t^2)^{3/2}} dt = \frac{eq_i}{2\pi\epsilon_0 v_e b}. \tag{2.13}$$

This implies that:

$$\alpha = \frac{b_0}{b} \qquad \text{in case } b \gg b_0, \tag{2.14}$$

where $b_0 = eq_i/2\pi\epsilon_0 m_e v_e^2$.

In case the approximation $b \gg b_0$ does not hold anymore, the deflection angle becomes larger and the energy lost in the collision becomes relevant.

As momentum conservation shall be fulfilled, the ion gains a momentum $\Delta p = m_e v_e \alpha$. The energy balance of the collision process leads to the ion gaining the energy $\Delta\mathcal{E}$ lost by the electron with energy $\mathcal{E}$:

$$\Delta\mathcal{E} = -\frac{(\Delta p)^2}{2m_p} = -\frac{m_e}{m_p}\left(\frac{b_0}{b}\right)^2\mathcal{E} \qquad \text{for } b >> b_0. \qquad (2.15)$$

In plasmas, a number of stochastic collisions occur and it is possible to perform a statistical estimation of the effects of multiple collisions.[2] As the direction of a single scattering is random, the mean deflection angle after many collisions is zero, but the mean square deflection angle process $\langle\xi^2\rangle$, during the time t, sums up to :

$$\langle\xi^2\rangle = 2\pi\int_{b_L}^{b_U}\left(\frac{b_0}{b}\right)^2 nv_e t\,db = 2\pi nv_e b_0^2 t\ln\left(\frac{b_U}{b_L}\right), \qquad (2.16)$$

where $2\pi nv_e b_0^2 t$ is the average number of encounters happened for the variation of the impact parameter db during time t (Fig. 2.6) and is proportional to the cross section [19].

The integral in equation (2.16) diverges logarithmically for asymptotic estimations of b (lower and upper), so we need to establish an estimation for the cut-off. The lower limit for the impact parameter arises from the Heisenberg uncertainty principle, and occurs when the distance b_L is less than half of de Broglie wavelength $\lambda_h = h/(2\pi m_e v)$ [20]:

$$b_{min} = \frac{\hbar}{2m_e v_T}, \qquad (2.17)$$

because at these scales we are entering the quantum world.

---

[2]In a completely ionised plasma one big scattering angle of the order of b_0 is far less likely to happen than cumulative small deflections that summed up make the same result. This is because $\lambda_D << b_0$ in fusion plasmas, so that multiple deflections are dominant.
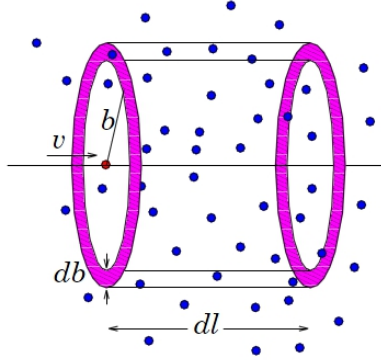
Figure 2.6: Variation of the impact parameter db

However if the de Broglie wavelength is smaller than b_0, the effective value of b_{min} is simply set to b_0. The upper bound shall be compatible with the shielding properties of the plasma (as it screens out the particle's Coulomb field) thus $b_{max} = \lambda_D$.

The integral in (2.16), is called the *Coulomb logarithm* $\ln(\Lambda)$ and represents the cumulative effect of all the Coulomb collisions within the range of the Debye sphere. Naming q_1 and q_2 the colliding charges, the resulting expression for the Coulomb logarithm $\ln(\Lambda)$ is given by [21]:

$$\ln(\Lambda) = \int_0^{\lambda_D} \frac{r\,dr}{r_0^2 + r^2}, \tag{2.18}$$

where $r_0 = \frac{q_1 q_2}{4\pi\varepsilon_0 \mu v^2}$ and μ is the *reduced mass* of the colliding particles m_1 m_2:

$$\mu = \frac{m_1 m_2}{m_1 + m_2} \tag{2.19}$$

As a consequence of this cut-off estimation for (2.16), particles outside of the region defined by the Debye sphere will not affect the electrostatic interaction during a collision. Typical magnetic fusion plasmas have $n\lambda_D^3 \approx 10^6$ which leads to $\ln \Lambda \approx 16$.

The effects of collisions can thus be included in the macroscopic model as a

friction force $\mathbf{F}_f$

$$\mathbf{F}_f = m_e \mathbf{v} \nu_c(v), \tag{2.20}$$

where $\nu_c(v)$ is the effective collision frequency for electrons.

For fast electrons,[3] the collision frequency $\nu_c^{ee}(v)$ depends also on the isotopic composition Z_{eff} of the plasma, which is defined as

$$Z_{eff} = \frac{\sum n_j Z_j^2}{\sum n_j Z_j}, \tag{2.21}$$

so that

$$\nu_c^{ee}(v) = \frac{e^4 \ln \Lambda n_e}{4\pi\epsilon_0 m_e^2 v^3}(2 + Z_{eff}). \tag{2.22}$$

The presence of impurities mostly resulting from sputtering and melting phenomena in the vessel FW and injected neutral atoms, would lead to modifications in the friction force $\mathbf{F}_f$. This plays a crucial role in runaway dynamics as will be discussed later.

---

[3]For a Maxwellian distribution, ion-electrons collisions dominate over electron-electron ones because of the larger inertia of ions. If electrons are sufficiently fast this is no longer valid and then electron-electron collisions also become relevant.

17

Chapter 3

Disruptions

3.1 Disruptive scenarios

Given the equilibrium configuration for a plasma in a tokamak, several issues regarding its stability need to be considered. In the toroidal coordinate system (r, θ, ϕ), a perturbation has the form:

$$\eta = \eta_0(r)e^{i(m\theta - n\phi)}. \tag{3.1}$$

Different combinations of m and n values identify different deformation that would arise in case the plasma equilibrium is perturbed. Macroscopic deformations (often called *MHD instabilities*) deal with modification of the geometrical modes of the plasma, whereas small scale phenomena related can generate microscopic instabilities.

As a consequence of MHD instabilities, a quick loss of the equilibrium configuration could be produced, hence a *disruption* occurs.
Such perturbation of the equilibrium causes the energy stored in the plasma to be released to surrounding structures, yielding potentially severe effects on the FW materials [22]. Moreover, a sudden change in position of the plasma column leads to rapid change in fluxes and then inductive currents (*eddy currents*) can affect the vacuum vessel components via the $J \times B$ force that exerts electro-mechanic stresses on the whole structure. For these reasons, disruptions represent one of

the main concerns for tokamak operation, especially in view of ITER and future fusion reactors.

3.1.1 Disruptive plasma instabilities

Causes behind MHD instabilities are many and not always straightforward to identify. Nevertheless, depending on the generation mechanism, it is possible to sketch a taxonomy for disruptive events.

Low-q disruptions

When the *safety factor*[1] is close to $q = 2$, the mode $m/n = 2/1$ can be excited and the interaction between the inner (hotter) and the outer (colder) part of the plasma, causes the temperature to decrease quickly, thus causing the plasma current to decay and destroy the confinement.

Further limitations are set by the *Kruskal-Shafranov limit* [23], that prescribes [2] values at $q > 1$.

Density limit disruptions

If the density n grows, the power radiated by the plasma increases as n^2. Thus the outer plasma would cool down very quickly, causing the effective plasma poloidal cross-section to shrink. The current density shows peaks that destabilize $q = 2$ modes and unstable *magnetic islands* appear.

---

[1] The safety factor q is a global parameter for plasma stability. Setting the angle offset between the poloidal position after a single toroidal turn as $\Delta\phi$, the safety factor is defined as:

$$q = \frac{\Delta\phi}{2\pi} \tag{3.2}$$

in order to take into account how many toroidal "laps" a particle needs to do single turn around the poloidal section. High q values stand for a more "safe" configuration in terms of confinement so particles are less likely to leave the plasma.

[2] As q depends on the poloidal flux ϕ function, such a condition is a fundamental constraint to consider when designing a tokamak device, because it influences the ratio between the applied magnetic fields, $q = \frac{aB_\phi}{RB_\theta} > 1$

VDEs *(Vertical Disruption Event)*

Due to the radial component of the magnetic fields used for controlling elongated plasmas, in case of bad positioning or a failure in the control system, the plasma column will move quickly upwards or downwards, impacting the vessel and causing serious damage to the machine diagnostics.

Troyon β limit disruptions

If the pressure gradient is increased locally, a change in the β parameter[3] is induced and consequently a local bulge arises in the plasma (*ballooning modes*). If the maximum total pressure allowed by the plasma configuration is exceeded, loss of confinement will inevitably occur.

Locked mode disruptions

When a plasma experiences a magnetic perturbation, especially in the current ramp-up phase, a *locked mode disruption* can occur. The physical mechanism responsible for mode locking is the braking effect of error fields or MHD modes that slow down and ultimately stop the plasma rotation [25]. Slowing down plasma rotation induces currents in the FW and thus creates an additional magnetic field B which causes the mode to grow in amplitude, worsening the magnetic confinement.

Internal Transport Barrier (ITB) disruptions

In order to achieve high performance plasmas, many tokamaks are operated in *H-mode* [26], an enhanced confinement scenario in which the energy confinement time is improved and the turbulences at the plasma edge but all disappeared. The improved performance of H-mode mainly results from the formation of an edge transport barrier (ETB) and further improvements can

---

[3]The ratio between plasma kinetic pressure and magnetic pressure is the β parameter:

$$\beta = \frac{nK_bT}{B^2/2\mu_0}. \tag{3.3}$$

Higher values for β indicate a good efficiency of the tokamak machine because that is related to the plasma temperature. It would also be an economically relevant parameter because of the high unitary cost for producing a suitable magnetic field. Estimates agree on a $\beta > 5\%$ in order to achieve an economically sustainable fusion reactor [24].

lead to the formation of an internal transport barrier (ITB). The presence of both ITB and ETB causes a relevant increase in confinement time, core temperature and pressure. The high pressure gradient present in ITB conditions excites unstable kink modes and ballooning modes, causing a loss of confinement on a short timescale and preserving high amounts of thermal energy up to the final quench [27].

3.1.2 Evolution of a disruption

From a temporal point of view, a disruptive process can be divided into three stages [28][29], as shown in Fig3.1:
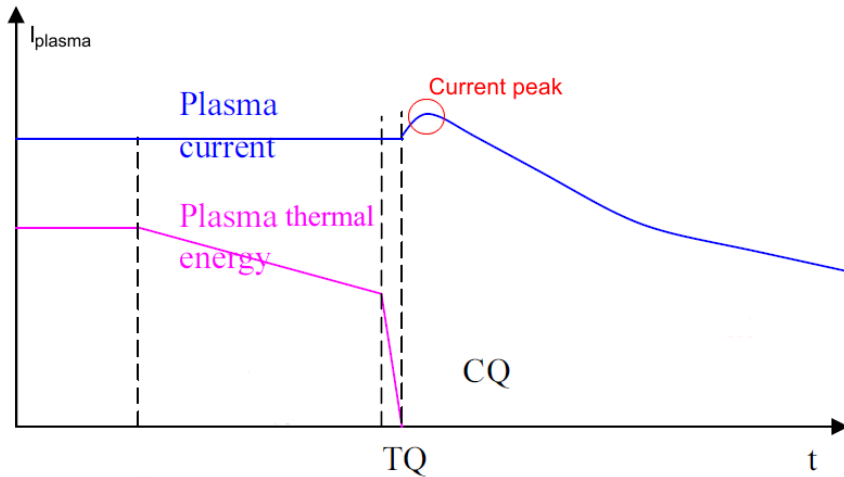
Figure 3.1: Evolution of plasma current and thermal energy during a disruption

The so-called *precursor stage* arises before the disruptive event effectively appears and it is characterised by a rise in the magnetohydrodynamic activity. Precursors are well visible oscillations of the poloidal magnetic field and electron temperature due the rotation of the magnetic islands. Precursors may be absent for disruptions due to instabilities with a high growth rate, for instance, for vertical displacement instabilities. This stage is characterized by a cooling of the outer plasma region while the plasma core remains essentially untouched as long as the $q = 2$ flux surface is unperturbed.

Once the loss of magnetic confinement becomes relevant, a rapid (several millisecond timescale) plasma thermal energy decay is experienced and a *thermal quench phase (TQ)* occurs. In this phase, severe consequences for the FW are expected, such as melting or sputtering phenomena due to high energy density reaching the FW in a very short time.

The heat load reaching the FW depends on the TQ duration τ_{TQ} but also on the surface irradiated by the energy released. While the amount of the original plasma thermal energy lost in a disruption is quite variable and depends strongly on the type of disruption (ranging from 20% in density limit disruption to 100% in VDEs), the other parameters are better known. For example, ITER [30] is expected to be stressed with τ_{TC} in $0.3 \div 3$ ms which leads to expected energy fluxes to FW during disruptions in the range of tens of GWm^{-2} [31][32]

As the thermal quench proceeds, impurity penetration in the plasma increases, therefore after the TQ occurs, the plasma is too cold ($T_e \approx 10eV$) and dirty to sustain a current. In this phase, the current density profile $j(r)$ has been shown to flatten, lowering the plasma inductance L and therefore, as magnetic energy conservation shall be fulfilled, the plasma current I shows a characteristic peak as shown in Fig.(3.1). After the transient effects cease, a *current quench (CQ)* inevitably appears due to the increased plasma resistivity. Furthermore, current quench decay (slower compared to TQ, $10 - 100$ milliseconds) depends on the impurity levels created during the TQ. The impurity level is linked both to Z_{eff} (2.21) and T_e, and since the *Spitzer resistivity* [33] η grows according to $\eta = 1.65 \times 10^{-9} Z_{eff} T_e^{-3/2} \ln \Lambda$, an augmented plasma resistivity is expected.

The presence of impurities accelerates the current decay by changing both Z_{eff} and the electron temperature T_e. Quicker CQs induce a loop voltage in PFC, generating eddy currents causing forces on the vessel.

3.1.3 Suppression and mitigation

As disruption phenomena are crucial, both from an engineering and theoretical perspective, for developing a safe and reliable fusion device combined with the need to avoid harmful damage to the machine, a number of techniques have been developed to counteract the effect of such events.

Figure 3.2: Effects of a disruption on Frascati Tokamak Upgrade (FTU) first wall (Photo credits: G.Mazzitelli)

Three main approaches are to be considered here and each of them has its own aim and importance: disruption avoidance, disruption mitigation and disruption prediction. In principle, a disruption avoidance scheme for a tokamak would be the safest, as it aims to avoid critical operational regimes for which disruptive phenomena are likely to happen [34]. This involves an extremely precise control of plasma pressure and current profiles and often it can not be achieved, as that would lead to an excessive shrinking of the operational conditions for the tokamak itself. However, in several cases, a reasonable avoidance of disruptive regimes can be done via a stabilization of MHD modes involved in the precursors phase [35][36]. Nevertheless, an effective avoidance in high performance regimes is often unavailable and mitigation of the disruption consequence would be a reasonable way to proceed. Although prediction-like techniques are adopted, the mitigation

phase remains indispensable once the disruptive event has been forecasted.

A possible solution for mitigating the disruption consequences deals with the redistribution of the heat flux over a surface as broad as possible during the thermal quench. Furthermore, accelerating the current quench decay is preferable from the point of view of reducing the energy deposition on PFCs but the current quench decay constant can not be too small without causing the rise of eddy currents in FW components: optimal values for current quench decay are therefore a trade-off between loads on FW and electromagnetic forces exerted on it.

Both of these strategies can be achieved by introducing a high-pressure puff of inert gases (usually neon or argon) because the gas injection reduces the FW surface thermal loads via radiative dissipation of nearly the entire plasma energy through isotropic radiation instead of concentrating thermal loads in smaller regions. Increasing impurities would also raise the Z_{eff} value, thus reducing the resistive timescale for the current quench duration. Moreover, poloidal *halo currents*[4] can be reduced if the plasma remains well centered in the vessel and the high-density impurity injection would also control the runaway electron generation, as will be discussed in the next section.

The first experiences in disruption mitigation on JET have been carried out through an injection valve (a slow one) injecting an amount of gas (usually helium, argon or neon) in the range of $9 \cdot 10^{21}$ - $2 \cdot 10^{22}$ atoms in approximately 50ms [37]. More recently, a faster *Disruption Mitigation Valve* (DMV) has been installed on JET and it is capable of better performances [38] in terms of quantity, mixing and injection rate of chosen suppression elements.

---

[4]Due to MHD instabilities, the plasma column can experience a displacement from its initial position, changing both the plasma cross-section and magnetic flux currents. Besides inductive effects due to changes in plasma area and position, a direct contact of plasma with the wall can also cause halo currents to flow into the FW following a minimal impedance path.

3.2 Runaway electrons

During the thermal quench, the plasma loses energy and cools down. As plasma conductivity depends on temperature as $\sigma \propto T^{3/2}$, a reduction in the plasma current is expected. The variation in current generates a magnetic field that tries to counteract the flux variation, which then results in a rise in the toroidal electric field E [39]. Besides the acceleration due to the field, a friction force also acts on the electrons because of their collision with other particles [39]. The model for friction force derived in (2.20), can be further refined re-writing the collision frequency $\nu_c(v)$ in terms of the *Chandrasekhar function* $G(x)$ [40] which is defined by:

$$G(x) = \frac{\phi(x) - x\phi(x)'}{2x^2},$$ (3.4)

where $\phi(\mathrm{x})$ is the error function

$$\phi(x) \equiv \frac{2}{\sqrt{\pi}} \int_0^x e^{-y^2} dy,$$ (3.5)

and ϕ' is its first derivative.

The friction force on an electron in a plasma 3.3 is proportional to $G(x)$, so it is a non-monotonic function of velocity: it increases at small velocities, as one would intuitively expect, but reaches a maximum and then decreases.

The acceleration due to the presence of the toroidal electric field E, balances the friction force at the *critical velocity* v_c [21]

$$v_c = \sqrt{\frac{3n_e e^3 \ln \Lambda}{4\pi \epsilon_0^2 m_e E}}.$$ (3.6)

Expression given in (3.6) is the velocity threshold above which the electrons will be continuosly accelerated away along the magnetic field lines. These electrons are called *runaway electrons* (*RE*s).

The inductive toroidal electric field E is related to the magnetic flux across
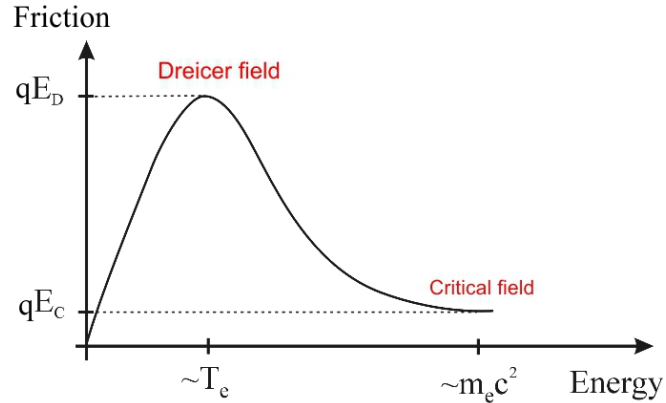
Figure 3.3: Friction force on an electron in a plasma as a function of particle energy

the poloidal cross-section $\Psi(t) = \int \mathbf{B} d\mathbf{S}$ according to the expression:

$$E(t) = -\frac{1}{2\pi R}\frac{d\Psi}{dt}. \tag{3.7}$$

The value for which the E field turns all electrons into REs is given by the *Dreicer field* E_D:

$$E_D = \frac{n_e e^3 \ln \Lambda}{4\pi\epsilon_0^2 T_e}, \tag{3.8}$$

obtained by setting v_c equal to the thermal velocity v_T.

The *critical field* has the form:

$$E_C = \frac{n_e e^3 \ln \Lambda}{4\pi\epsilon_0^2 m_e c^2}. \tag{3.9}$$

For each field $E > E_c$, REs are generated. REs generation generally occurs by either lowering E_C, as in early stage plasmas during the current ramp-up phase, or increasing the toroidal field E, as in disruptive scenarios. It is important to point out that the expression for the critical velocity v_c for runaways (3.6) can be rewritten in terms of the Dreicer field E_D (3.8),

$$v_c = \left(\frac{T_e}{m}\right)^{1/2}\left(\frac{E_D}{E}\right)^{1/2}. \tag{3.10}$$

3.2.1 Primary runaway generation

Assuming the toroidal field E_ϕ to be coincident with the parallel component of the electric field $E_\parallel$, if the inequality

$$E_\phi > E_C \tag{3.11}$$

holds, a certain amount of electrons will enter the runaway regime and the resulting net flux of particles will evolve according to the evolution equation [41] for the density of REs n_{RE}^I:

$$\frac{dn_{RE}^I}{dt} = n_e \nu^{ee} \left(\frac{E_D}{E_\parallel} \right)^{\frac{3(1+Z_{eff})}{16}} \exp \left(\frac{-E_D}{E_\parallel} - \sqrt{\frac{(1+Z_{eff})E_D}{E_\parallel}} \right), \tag{3.12}$$

where Z_{eff} comes from (2.21) and $n_e \nu^{ee} = \frac{n_e}{\tau} \left(\frac{m_e c^2}{2T_e} \right)^{3/2}$ takes into account the electron-electron collisions. This is the most fundamental generation mechanism and it is known as *primary generation* or *Dreicer generation*.

3.2.2 Secondary runaway generation

If a close collision between a runaway and a thermal electron occurs, the probability that both electrons involved will have a sufficient energy to overcome the critical energy/velocity is high.

Also, it should be noted in this scenario, the "ordinary" electron would be kicked into the runaway region and the probability of another collision increases. Having two electrons in place of one, they could again collide with other electrons in the plasma. This means that, in the long run, a sort of electronic chain reaction takes place and an exponential growth of the number of REs is experienced. This mechanism is called *avalanche runaway* generation or *secondary generation mechanism* because starting from a seed population of runaways provided by the Dreicer mechanism, it increases the global runaway population.

It is important to point out that the avalanche mechanism does not generate

primary runaways but is triggered both by Dreicer and hot tail REs; those can be seen as the "seeds" of the secondary generation. In ITER even additional seeding sources would be relevant, such as Compton scattering by activated FW materials [42]. The avalanche process is the most relevant source of REs during a major disruption in ITER-sized machines, because the number of successive runaways doubling is proportional to the plasma current I_p, according to [43]:

$$\frac{I_p}{I_{Alfven} \ln \Lambda},\tag{3.13}$$

where $I_{Alfven} = \frac{4\pi m_e}{c(\mu_0 e)} = 17kA$.

The equation governing the time evolution of avalanche runaway production has the form [43]:

$$\frac{1}{n_r}\frac{dn_{RUN}^{II}}{dt} = \frac{E_\parallel/E_C - 1}{\tau_{ee} \ln \Lambda}\sqrt{\frac{\pi\varphi}{3(Z_{eff}+5)}}\left(1 - \frac{E_c}{E_\parallel} + \frac{4\pi(Z_{eff}+1)^2}{3\varphi(Z_{eff}+5)(E_\parallel^2/E_c^2 + 4/\varphi^2 - 1)}\right),\tag{3.14}$$

where $\varphi = 1 - 1.46\sqrt{\varepsilon} + 1.72\varepsilon$ and $\varepsilon = r/R$ is the inverse aspect ratio. τ_{ee} is the electron collision time $\tau_{ee} = 4\pi\varepsilon_0 m_e^2 c^3/(n_e e^4 \ln \Lambda)$.

3.3 Runaway loss and suppression

3.3.1 Thermalization and radiative processes

So far, a tacit assumption has been the absence of loss mechanisms for REs and, therefore, no sink terms in the evolution equation have been introduced. Models for losses can be divided into two categories depending on whether the REs are extinguished by radiation/thermalization or by crashing into the FW.

Due to their very high energy they cannot thermalize as quickly as the low energy electrons, since only a $1MeV$ electron in a $1.7 \cdot 10^{20} m^{-3}$ background electron density requires 30 ms to thermalize [44]. Classical thermalization loss mechanisms associated with collisions with ions or even other electrons are negligible

because, in steady conditions[5], an interaction between REs is not very likely to occur. In this framework, radiative losses due to a change in the acceleration of the RE beam becomes much more relevant. Both collision processes and the gyration/twisting motion which the electrons are subject to, generate dissipative processes through the radiation emission (*Bremsstrahlung*) and, in case a (non-relativistic) charge moves into a magnetic field, *cyclotron radiation* is emitted. At very high velocities relativistic effects have to be taken into account, switching the radiative loss to the so called *synchrotron radiation* (Fig.3.4), emitted in a cone along the direction of motion.
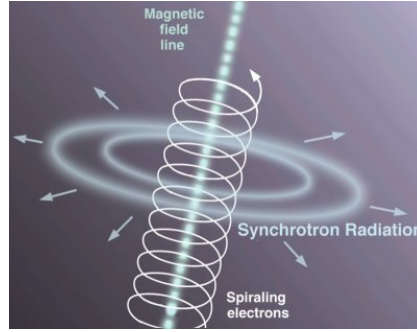
Figure 3.4: Synchrotron radiation emission scheme (relativistic effects not included)

An estimation of the radiated power due to synchrotron radiation emitted by runaway electrons is given by :

$$P_{syn} = \frac{2r_e m_e^2 c^3}{3x^2} \beta^4 \gamma^4 \tag{3.15}$$

where $r_e = e^2/4\pi\epsilon_0 m_e c^3 = 2.82 \cdot 10^{-15} m$ is the classical electron radius, $\beta = v/c$ the speed in units of c, γ the relativistic Lorenz factor[6] and x the curvature radius of the electron's trajectory.

---

[5]Even in case REs have been already slowed down, collisions relevance is questionable and constrained to the very end of the disruption.

[6]The *relativistic Lorenz factor* arises from the Lorentz trasformation used in the special relativity formalism and is a measure of how relevant relativistic effects are in a chosen reference frame. $\gamma = \frac{1}{\sqrt{1-\beta^2}}$

3.3.2 Radial losses

In their gyration motion along field lines, REs can be flung away to outer lines as a consequence of a collision, and this can generate a decrease of their number due to losses to the FW. This process is closely proportional to the occurence of collisions in the plasma and since REs have a very low collisionality, it can essentially be neglected.
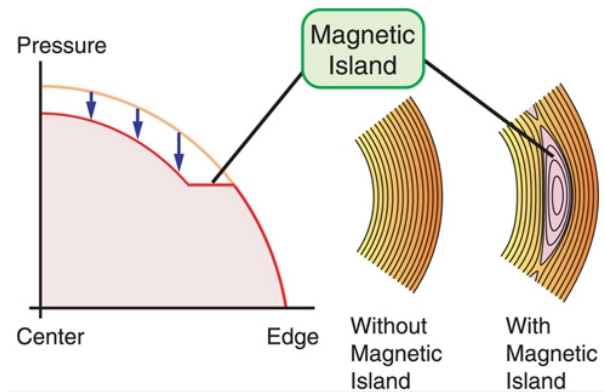
Figure 3.5: Magnetic islands effects on magnetic field surfaces

Although REs are not very sensitive to electrostatic turbulences due to their high velocities, they are influenced by magnetic perturbations. Magnetic perturbations are the predominant cause for loss of REs, as they are acting on an intrinsically unstable [45] configuration of the nested flux surfaces. Even small perturbations in B trigger the development of magnetic sub-structures, called *magnetic islands* (Fig.3.5). The spontaneous onset of magnetic islands in the tokamak plasma leads to an increased heat and particle transport and worsens the energy confinement, flattening temperature and density within these regions and even provokes the loss of plasma when the islands become too big and start interfering with the overall magnetic field, introducing stochastic behaviour [46][47].

In such stochastic scenario, the influence of magnetic oscillations on the runaway electrons can be reformulated as a diffusive process [48][49][50], obeying an evolution equation of the form:

$$\frac{\partial n_{run}}{\partial t} = \frac{1}{r}\frac{\partial}{\partial r} r D_{RR} \frac{\partial n_{run}}{\partial r}, \tag{3.16}$$

where r is the radius, D_{RR} is the *Rechester-Rosenbluth diffusion coefficient* estimated as $D_{RR} = \pi q v_{\parallel} R (\frac{\delta B}{B})^2$,[43] [51] taking into consideration the influence of the magnetic field perturbation $\frac{\delta B}{B}$ on the reduction of plasma confinement.

Chapter 4

Modeling and simulation

4.1 Modeling

Runaway electrons are energetic and highly harmful to the tokamak hardware. Therefore their generation must be avoided or significantly reduced if the aim is to produce energy in a reliable and steady manner. The first step to physically understand the generation and the evolution of the phenomenon is to set up a reasonable, coherent and easy-to-handle mathematical model.

4.1.1 Model equations

As kinetic modeling of REs is very challenging and expensive from a computational point of view, it is useful to simplify the model focusing only on the amount of current carried by the REs.

The temporal evolution of the runaway electron density $n_{run}(r, t)$ is changing due to a number of different effects and generation mechanisms. Generation, in fact, occurs due to the Dreicer mechanism (3.12) and the avalanche (or secondary) mechanism (3.14). In addition, irradiated FW components can emit a large amount of gamma radiation and collisions between the γ photons and plasma electrons can drive the latter into the runaway region.
A sink term due to radial diffusion, with the consequent redistribution of REs

modeled through the Rechester-Rosenbluth coefficient (3.16), must be taken into account. Neglecting, for simplicity, the gamma-induced runaway electrons and the sink terms, the equation governing the runaway electron density time evolution $\left(\frac{dn_{RE}}{dt}\right)$ is made up of the terms :

$$\left(\frac{dn_{RE}}{dt}\right) = \left(\frac{dn_{RE}}{dt}\right)^{Dreicer} + \left(\frac{dn_{RE}}{dt}\right)^{Avalanche} \quad (4.1)$$

Runaway production is closely related both to the electric field E and to the collisions occurring in the plasma. Another set of equations should therefore be added to the model to guarantee a balance of energies for all the species present in a plasma in order to describe the plasma cooling process.

The thermal energy of electrons, for example, is affected by diffusion (according to the heat diffusion coefficient χ) but also increases due to ohmic power P_{OH} and the energy transferred by the collisions with deuterium atoms P_c^{eD} and impurities P_c^{eZ}. Losses in thermal energy, for electrons, originates from line radiation[1] P_l, bremsstrahlung phenomena P_{Br} and from ionization energy loss P_{ion}. The evolution of the thermal electron energy is therefore of the form :

$$\frac{3}{2}\frac{\partial(n_e T_e)}{\partial t} = \frac{3n_e}{2r}\frac{\partial}{\partial r}\left(\chi r\frac{\partial T_e}{\partial r}\right) + P_{OH} + P_c^{eD} + P_c^{eZ} - P_{Br} - P_l - P_{ion} \quad (4.2)$$

It is also necessary to write down an analogous equation for the ions. In these equations ohmic heating and radiative losses do not appear and heat exchange times are generally different. The extensive form of the collisional terms could be retrieved from [21].

For deuterium and impurities, respectively, the equations become :

$$\frac{3}{2}\frac{\partial(n_D T_D)}{\partial t} = \frac{3n_D}{2r}\frac{\partial}{\partial r}\left(\chi r\frac{\partial T_D}{\partial r}\right) + P_c^{De} + P_c^{DZ} \quad (4.3)$$

---

[1]The line radiation is the sum of the radiation for each charge state and depends on the radiation rates. Radiation data used in this work, are extracted from the ADAS database[52]

$$\frac{3}{2}\frac{\partial(n_Z T_Z)}{\partial t} = \frac{3n_Z}{2r}\frac{\partial}{\partial r}\left(\chi r\frac{\partial T_Z}{\partial r}\right) + P_c^{Ze} + P_c^{ZD} \tag{4.4}$$

The heat diffusion coefficient χ is assumed to be constant and equal to $1 m^2/s$ in this work.

The time evolution of the charge state populations are described using the rate equations. The final equation to be included into the model takes into account the fact that the electric field varies in both time and space. Deriving a toroidal version of the Maxwell equation $\nabla^2 E = \mu_0 \frac{\partial J}{\partial t}$ and combining it with Ohm's law, one can obtain the equation :

$$\frac{1}{r}\frac{\partial}{\partial r}\left(r\frac{\partial E}{\partial r}\right) = \mu_0 \frac{\partial}{\partial t}(\sigma_\parallel E + n_{RE}ec) \tag{4.5}$$

where $\sigma_\parallel$ is the toroidal conductivity.

4.1.2   The GO code

To solve the system of equations (4.1-4.5), a MATLAB code has been developed under the working name of GO [53] and developed further in [52]. The algorithm implemented to solve (4.1),(4.2),(4.3) and (4.4) adopts a discretization based on a *Forward-Time Central-Space (FTCS)* scheme: the low heat coefficient suggested the use of an Euler-based method in time to take advantage of the computational inexpensiveness of the method and avoid stability problems in such parabolic-like equations [54].

For the electric field diffusion equation (4.5), the assumption of low diffusivity is no longer valid. Thus an implicit *Crank-Nicholson* discretization scheme has been used, as it guarantees a stable solution.
The use of an implicit method affects the computational time needed, as it implies solving a (nonlinear) system of equations for each step, but such a drawback is an inescapable by-product when seeking to estabilish a stable solution [55].

4.2 Simulations

4.2.1 Data and scenarios

Once the mathematical model has been set up, the next step is to perform simulations aimed at understanding the role of different impurities in the dynamics of the runaway electrons. The question is how different the runaway electron behaviour is in the presence of carbon and beryllium walls. Such a question has gained increasing relevance due to the significant impact of the new beryllium *ITER-like wall (ILW)*, installed at JET, on the plasma itself [56]. The presence of beryllium, in fact, affects the way the energy is radiated during a disruption, changing the evolution of the temperatures and thermal quench with respect to the carbon wall measurements.
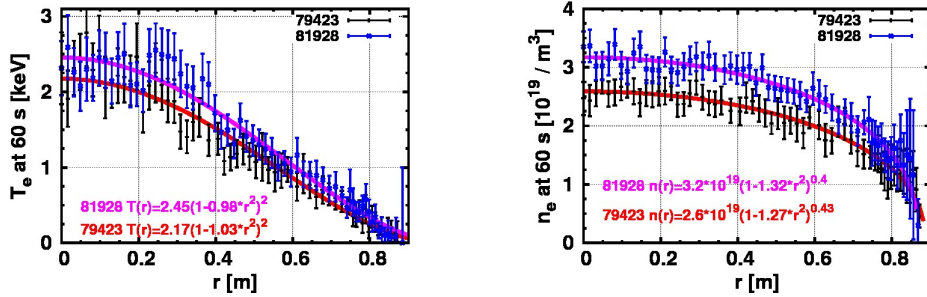
Figure 4.1: Experimental data and fits for electron (left) temperature and (right) density measured for #79423 (red) and #81928 (magenta) [5]

.

To investigate the effect of the ILW on the runaway generation rates, two JET discharges with similar parameters but different wall composition have been compared. The chosen discharges are #79423 (carbon wall discharge) and #81928 (ILW). Experimental data for temperature and density profiles relative to the discharges, are shown in Fig.4.1 together with the analytical fit (in the general form $\alpha(1-\beta r^2)^\gamma$, see Table 4.1) used to simplify the numerical simulations. Simulations have been carried out turning off loss mechanisms, focusing the attention on the effects of the different walls on runaway generation mechanisms.

Table 4.1: Initial plasma parameters used in the simulation

	Scenario ITER-like wall	Carbon wall
Duration (ms)	80	80
Plasma current I (MA)	1.93	2
Major radius R (m)	3	3
Radius of the conductive wall b (m)	1.3	1.3
Minor radius a (m)	0.88	0.88
Elongation k	1.2	1.2
Magnetic field B (T)	2	2
Coulomb logarithm $\ln \Lambda$	23.2	23.2
T profile	$(1 - 0.982(ax)^2)^2$	$(1 - 1.031(ax)^2)^2$
n profile	$(1 - 1.322(ax)^2)^{0.3}$	$(1 - 1.271(ax)^2)^{0.4}$
Initial T	1.5 keV	2.2 keV

Measurements performed during the full disruptive phase result sometimes in inaccurate data, so direct comparisons between simulation and experimental data in some cases are not possible. Also, as will be more clear later on, several crucial parameters, e.g. the mixing efficiency for the injected impurities and the background impurity levels are not known. In these cases reasonable assumptions and parameter scans were performed to assess their impact on the simulations.

4.2.2 Exponential decay scenario

In the first scenario, a simplified evolution of a plasma disruption was considered. The evolution of the temperature was assumed to have an exponential time dependence close to the experimental data retrieved for electron temperature T_e. If T_0 is the initial temperature, T_f is the final temperature, and t_0 is the decay constant given in Table 4.1, the temperature evolves according to:

$$T_e(t, x) = T_f(x) + [T_0 - T_f(x)]exp(-t/t_0). \qquad (4.6)$$

The first scan performed is aimed at understanding what is changing in the post-disruption plasma current I. This is achieved by running a GO simulation

using different values for the final temperature T_f both in ITER-like wall (#81928) and carbon wall (#79423) cases. The evolution of the runaway current is also considered and presented in Figs.(4.2)-(4.5). The range of final temperatures considered for is $5 - 200$ eV.

The simulations show that the plasma resistive current is substituted by runaways and confirms that lower final temperature allows the current to reach the steady state in a shorter time (the current quench is short). Moreover, the percentage of the total current converted into runaways is different for different final temperatures: lowering final temperature triggers a higher production of runaways and the current quench becomes more rapid.

Figure 4.2: Currents - Exponential decay scenario,#81928 (ITER-like wall), (left) $T_{final} = 5$ eV, (right) $T_{final} = 20$ eV

Similar evolution can be observed for both reference discharges used, even if the #79423 case at $5eV$ final temperature, the total current shows a lower drop, becoming stabilized above 1.5 MA, while the ILW discharge showed a drop under 1.5 MA. This is due to the slightly higher plasma current in the discharge #79423 (2 MA against 1.93 MA for #81928).

The relatively low generation of runaways with higher final temperature is confirmed by scanning a broad range of final temperatures and analyzing the runaway current density. As figure Fig.4.4 shows, there is a higher runaway current density at lower temperature. Ultimately, increasing the final temperature
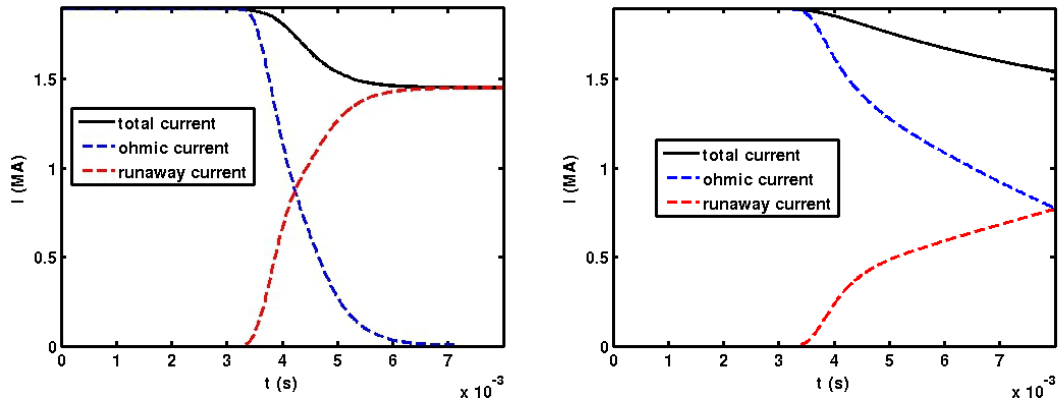
37
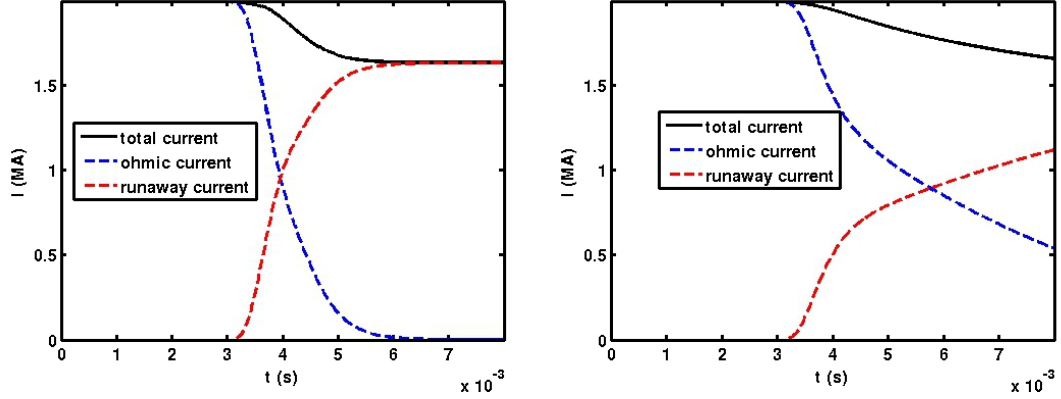
Figure 4.3: Currents - Exponential decay scenario, #79423 (carbon wall), (left) $T_{final} = 5$ eV, (right) $T_{final} = 20$ eV

parameter, the runaway current density becomes extremely weak. Slower current decays generated by higher final temperatures, are less likely to go over the critical electric field at which runaway electrons are generated, and then the runaway production and the density are both lower than the expected values for lower final electron temperatures.

The temperature affects also the spatial distribution of the runaway current density (Fig.4.5). Lower final temperatures let the runaways to be created further away from the axis than when T_f is higher and the runaway current appears more concentrated around the centre.

A thorough analysis has been carried out for significant parameters such as density to assess their impact on the RE simulation: densities have been scanned in the range from 0.05 to 0.5 and different profiles have been implemented (see Table 1 in Appendix A). The outcomes of the simulation resulted not to be very dependent on the profiles tried.

4.2.3 Injection scenario

A more elaborate and realistic scenario for RE simulation has to include the impurity ionization and radiation processes and the impurity density profile. A reasonable choice could be to use the pre-disruption electron density profile shape.
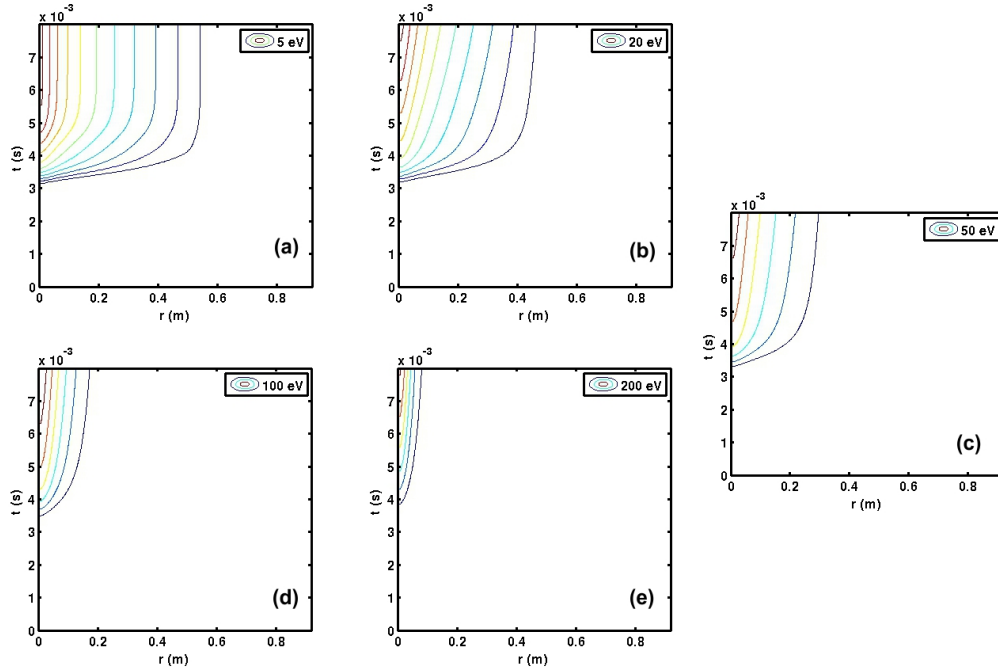
Figure 4.4: Runaway current density vs radius and time, Exponential decay scenario,#79423 discharge - (a) $T_{final} = 5$ eV, (b) $T_{final} = 20$ eV, (c) $T_{final} = 50$ eV, (d) $T_{final} = 100$ eV, (e) $T_{final} = 200$ eV
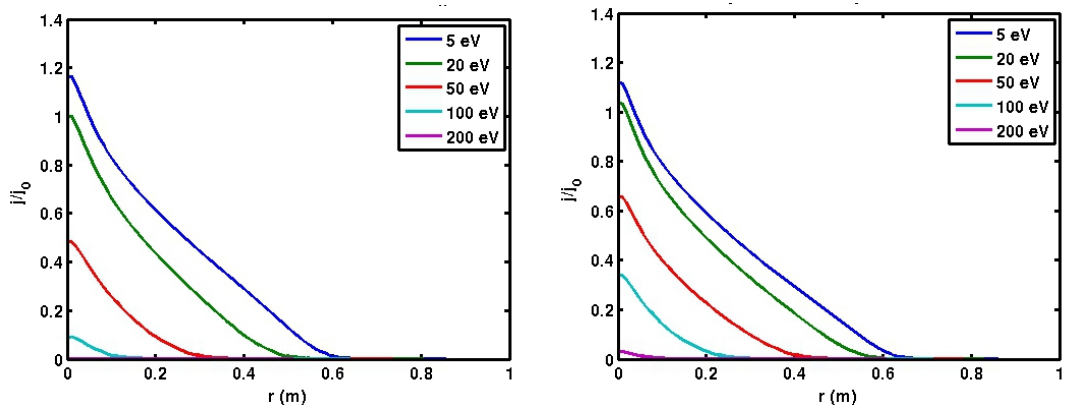
Figure 4.5: Final runaway current density, exponential decay scenario - (left) #81928, (right) #79423

All simulations with impurity injection have been performed using that reference shape.

4.2.3.1 Injection time

The first impurity injection investigated through the simulations was the argon injection. The density distribution for an impurity introduced into the plasma is assumed to follow an exponential law:

$$n_Z(t, x) = n_Z^r(x)[1 - \exp(-t/t_{inj})] \qquad (4.7)$$

where, n_Z^r is the radial profile for the generic impurity species Z and t_{inj} indicates the injection time constant. In an injection scenario the preliminary parameter for which a scan should be performed is injection time t_{inj}, intended as the time needed to puff a fixed amount of argon gas inside the plasma. This kind of analysis was performed for both the #81928 and #79423 discharges. A scan over injection times t_{inj} was carried out over several orders of magnitude, with t_{inj} assuming values in the range $[10^{-5}, 10^{-4}, 10^{-3}, 10^{-2.5}, 10^{-2}]$ seconds.
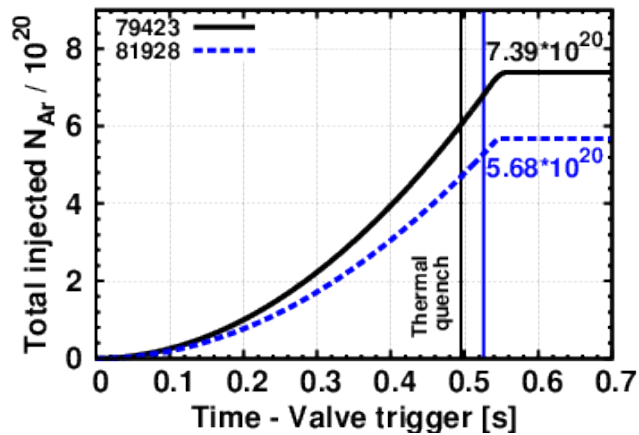
Figure 4.6: Total injected argon versus valve trigger time. Adapted from [5]

Setting an argon level of 10% (with respect to total pre-disruption electron density) in the #79423 discharge, independently on how fast the argon is injected,

nothing changed over a simulation lasting for 110 ms. The same behaviour has been seen for the #81928 discharge. This is due to the fact that the level of argon used is not enough to sufficiently perturb the plasma state, as the RE production is negligible.

To identify the role of the injection time, a simulation has been performed increasing the argon level to 30%. The relevant temperature dynamics is visible already in the first few milliseconds. Injecting 30% of argon influences the plasma considerably. At one extreme of the timescale there is the fast injection case, as in figure 4.7 (left), which generates a sudden drop in temperature (in this specific case we can observe a reduction of 80% of the initial temperature) and leads to a complete cooling of the plasma.
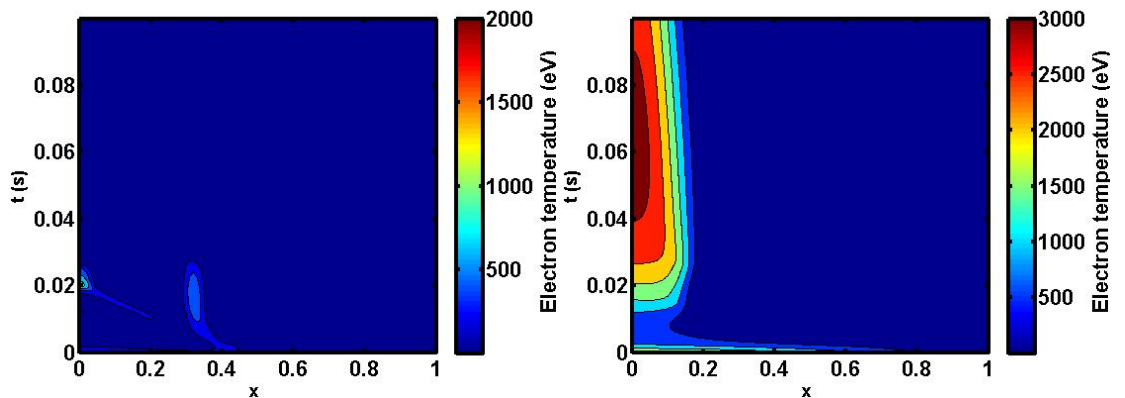
Figure 4.7: Discharge #79423. Electron temperature with $n_{Ar}/n_e = 0.3$, with $x = r/a$. (left) Injection time : 10^{-5} s, (right) Injection time : 10^{-2} s

On the other hand, injecting the same quantity of argon during a 0.01 second interval would only cause a small decrease in temperature as a consequence of direct contact of the injected atoms with the hot plasma (Fig.4.7(right)).

As for the levels of runaway current, simulations carried over the chosen values for injection time show that the current carried by REs are decreasing if the speed of injection rises (Fig.4.8). A possible explanation for this could be given on the basis of the ionization processes occurring: faster injected atoms lead to more effective plasma cooling. If the injection time is long enough, Ohmic heating will counteract the radiative cooling.
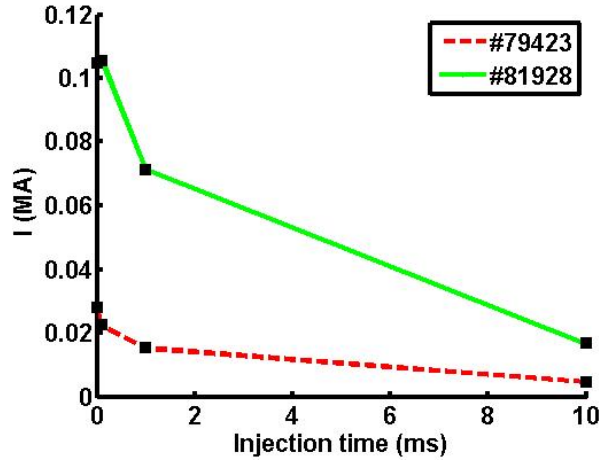
Figure 4.8: Runaway currents (maximum) versus different values of t_{inj}, argon impurity level $n_{Ar}/n_e = 0.1$

4.2.4 Pure argon injection

This section describes the results of simulations where a scan over the amount of argon impurities injected into the plasma was performed.

Given that simulations in the previous paragraph suggests that it is not reasonable to consider an excessively quick gas injection process, the order of magnitude of the injection constant has to be chosen in the $[10^{-4}, 10^{-3}]$ range. Here the value $t_{inj} = 3 \cdot 10^{-4} s$ was selected [57]. Also in these simulations, the amount of injected gas was chosen to represent less than the total number density of electrons. The profile shape of the injected argon has been assumed to be equal to the electron density profile shape.

Experimental data was used to determine a reasonable impurity density range from which to scan for injected argon. For #79423 and #81928, the total amount of injected argon atoms were $7.39 \cdot 10^{20}$ and $5.68 \cdot 10^{20}$, respectively. The initial electron density was roughly $3.11 \cdot 10^{19} m^{-3}$ and $2.8 \cdot 10^{19} m^{-3}$, respectively for #81928 and #79423. But given that knowledge about the impurity injection efficiency and penetration dynamics is basically lacking, however a set of additional assumptions had to be made.

Let us define the *assimilation rate* (or *mixing efficiency*) as the fraction N_{into} of the injected gas that can effectively reach the plasma over the total injected gas N_{total}:

$$\eta_{assimilation} = \frac{N_{into}}{N_{total}}.$$

A reasonable value for assimilation lies around 30% and consequently injection of argon should be in the range $0.2-0.5$ times the electron density. As one can see in Figure (4.9) (left) injecting only 10% argon would not lead to any substantial runaway production (only 4.5 kA of REs were produced). The temperature drop is not intense enough (Fig.4.9) (right) to cool down the plasma in an irreversible way because the ohmic heating of the plasma counteracts the drop in energy.

Only a small fraction of the energy is lost in this process as the current is barely influenced and the temperature after the drop goes up, allowing the plasma to recover from the cooling shock it received with the injection.
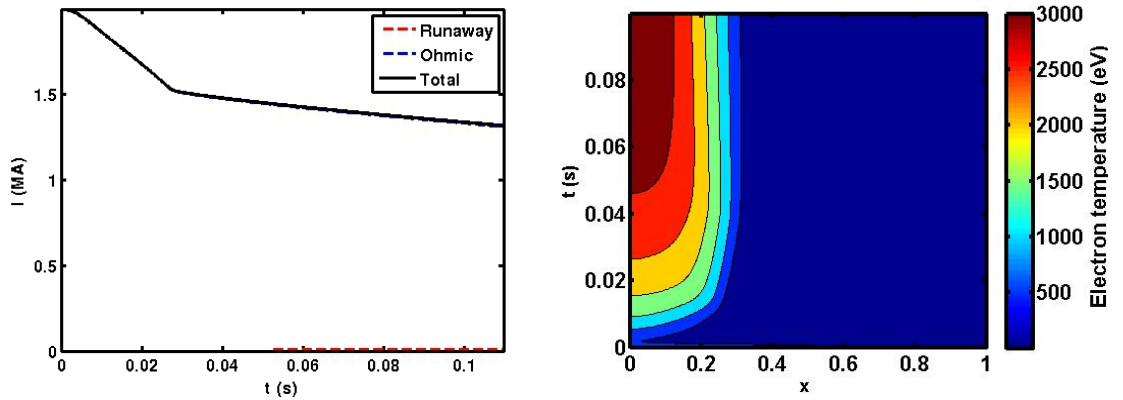
Figure 4.9: Discharge #79423 $n_{Ar}/n_e = 0.1$, (left) Currents, (right) Electron temperature on axis

Increasing the quantity of argon injected to 30% (Fig.4.10) (left) something different happens: runaways are now produced in a quantity that is close to that observed ($600kA$ in #79423 and less than $100kA$ in #81928). The temperature behavior is also different: a sharp and deep drop in T_e allows the resistivity to grow and the ohmic current will therefore decrease as more runaway electrons are

produced.

Increasing the value of the injected argon even more to 50% (Fig.4.10) (right) affects the plasma even more: the initial plasma current is converted to a 0.68 MA current while the ohmic current decreases and a characteristic current "plateau" is formed after approximately 22 ms.
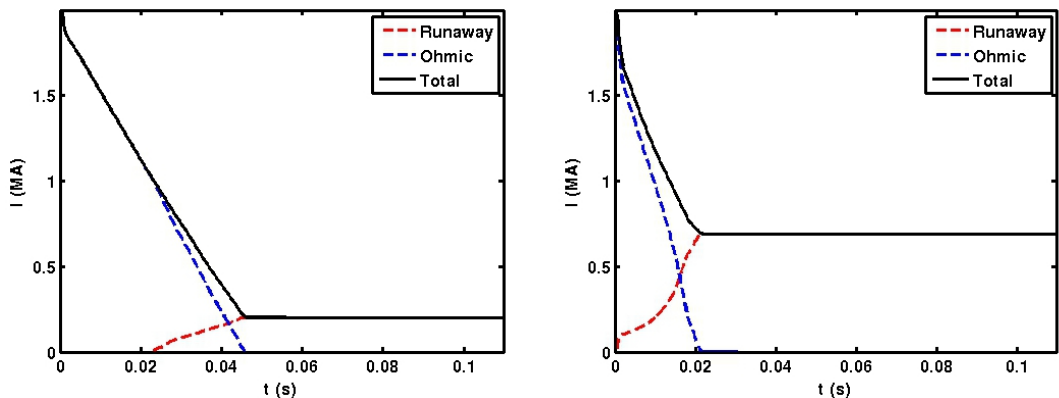
Figure 4.10: Discharge #79423, (left) Current for $n_{Ar}/n_e = 0.3$, (right) Current for $n_{Ar}/n_e = 0.5$.

Simulations carried out by increasing the value of the injected argon for discharge #81928, demonstrated a similar general trend (Fig.4.11): while plasma current is lower, the runaway current generation is more pronounced when increasing argon levels.

To understand different phenomena in terms of runaway generation, it is necessary to enrich the model and investigate the effects of the argon injection in the presence of wall impurities (carbon and beryllium). As a direct consequence of the disruptive events, the PFCs suffer sputtering and melting of particles composing the FW materials and this does have an impact on the composition of the background impurity levels. Because of different walls in #79423 (carbon) and #81928 (beryllium), and considering also the similarity of the initial plasma parameters, a comparison of these two scenarios will be discussed in the following.
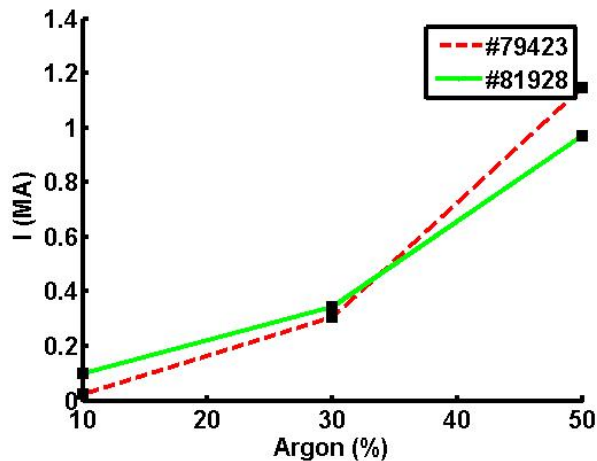
Figure 4.11: Runaway current for different injected argon levels, discharges #79423 and #81928.

4.2.5 Argon and carbon/beryllium impurities

Simulations using different argon levels, have been used to find a reasonable range to scan, leading to the conclusion that, for carbon (and later beryllium) impurities, it is useful to carry out a scan on a matrix for concentrations along $C = \{5\%, 10\%\}$ and $Ar = \{20\%, 50\%\}$. Both argon and carbon impurities have an impact on the runaway production by themselves.

	Argon 20%	Argon 50%
Carbon 0%	0.421	1.146
Carbon 5%	0.397	1.166
Carbon 10%	0.390	1.167

Table 4.2: Discharge #79423 - Runaway current production (in MA) for different Ar+C mixtures.

As can be seen in Fig.(4.12), increasing the level of argon injected with from 20% to 50%, 5% carbon in the background, the current quench time is significantly reduced from 0.12 ms to less than 0.02 ms. In principle, this should be good news in the perspective of disruption mitigation because a shorter current quench would imply a successful reduction of halo currents and thermal loads on the FW. Unfortunately, the tradeoff is a higher production of runaway current (Tab.4.2).

While in the 20% case the runaway current estimate is $I \approx 0.45$ MA, increasing the level of argon would result in a dramatically higher level of REs produced ($I \approx 1.167$ MA).
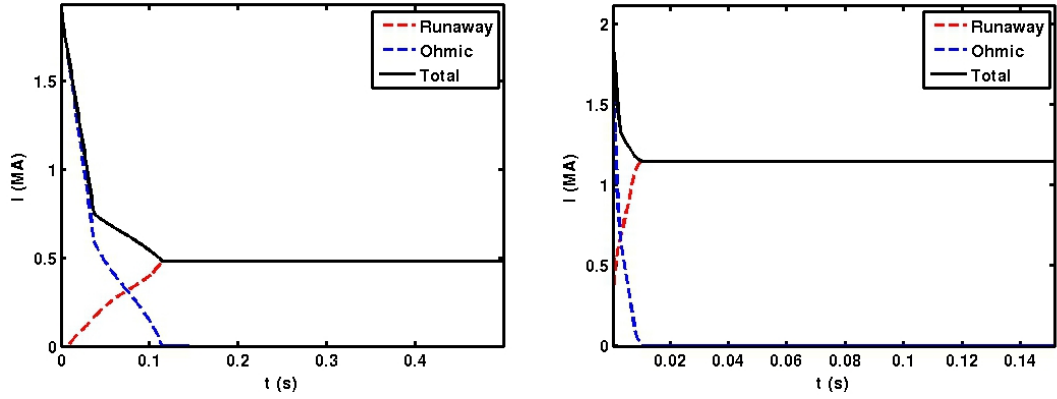
Figure 4.12: Discharge #79423, $n_C/n_e = 0.05$. Currents for (left) $n_{Ar}/n_e = 0.2$,(right) $n_{Ar}/n_e = 0.5$

Also, the evolution of the electron temperature tells two different stories for different argon levels: in Fig.(4.13) (left) the profile of the electron temperature on axis decreases at a slow rate, whereas in Fig.(4.13) (right), where more argon is injected, the cooling of the core is immediate.
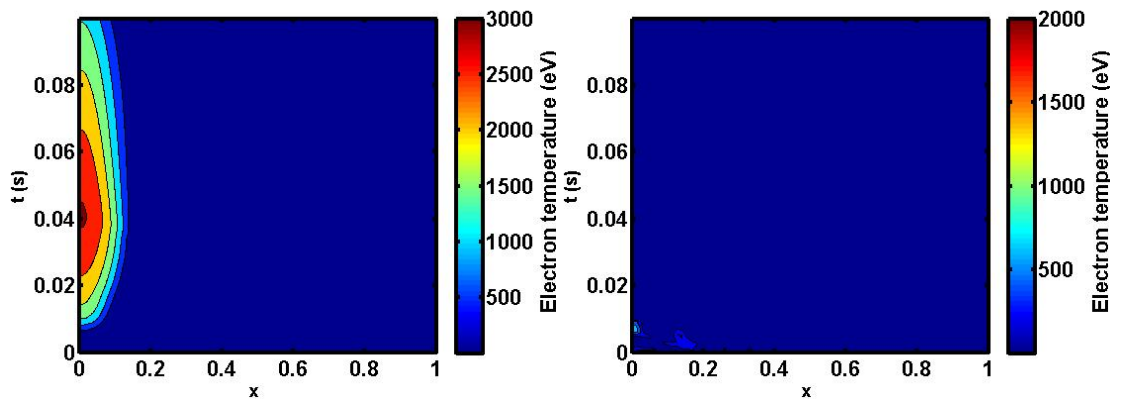
Figure 4.13: Discharge #79423, $n_C/n_e = 0.05$ - Electron temperature (left) $n_{Ar}/n_e = 0.2$,(right) $n_{Ar}/n_e = 0.5$

To understand the role of the carbon, one can inspect different current densities generated both without carbon and then by adding different background carbon impurities. The carbon-free scenario (Fig.4.14)(left) differs from the carbon scenario (Fig.4.14)(right) due to the large increase in the current density produced by the presence of even a small quantity of carbon impurities. The presence of carbon radiates a portion of the energy, which also affects the electron temperature which shows a peak at the beginning when the generation of runaways occurs (Fig.4.15(right)). Different behaviour can be observed handling the scenario with only pure argon (Fig.4.15(left)): the current drop occurs rapidly and runaways are scarcely produced (Tab.4.2).
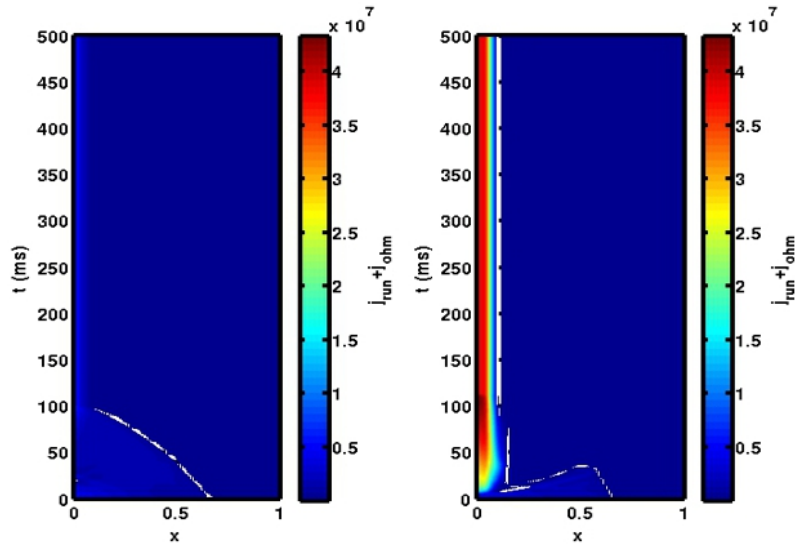
Figure 4.14: Discharge #79423, Current density comparison between pure argon (left) and argon + carbon (right), $n_{Ar}/n_e = 0.2$, $n_C/n_e = 0.05$

In case the wall impurity is beryllium, the difference between the scenarios with and without a 5% amount of beryllium is less evident (Fig.4.16) and only a small difference in terms of runaway production can be seen (see Tab.(4.3)). It is difficult to find a general explanation for the different scenarios just comparing two single discharges with similar, but not equal parameters because the nonlinearity of the system acts strongly to broaden the initial gap in term of initial density, temperature and profile shape, causing a total different evolution of the
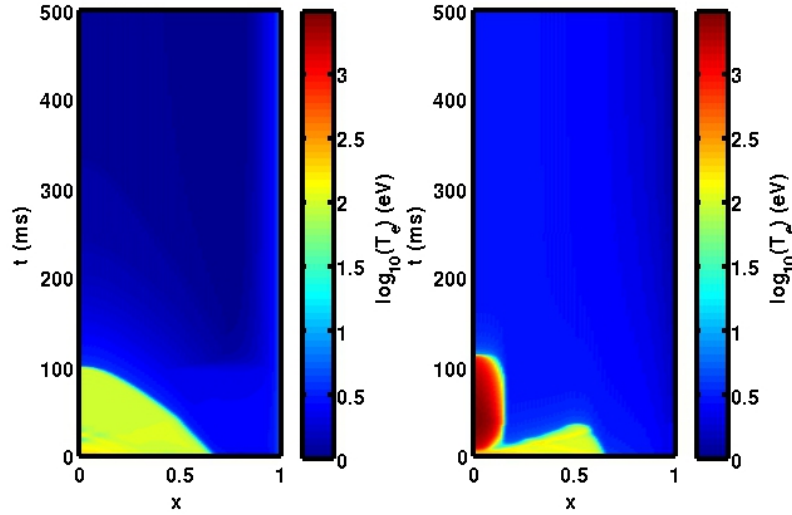
Figure 4.15: Discharge #79423, Electron temperature comparison between pure argon (left) and argon+5% carbon (right), $n_{Ar}/n_e = 0.2$, $n_C/n_e = 0.05$

whole system. However, also in the case of beryllium impurities, the general trend of REs is decreasing.

A possible way to grasp the effects of the different materials used for gas injection, would be to refine the analysis to consider also the role of runaway generation mechanisms rather than the mere final total runaway current.
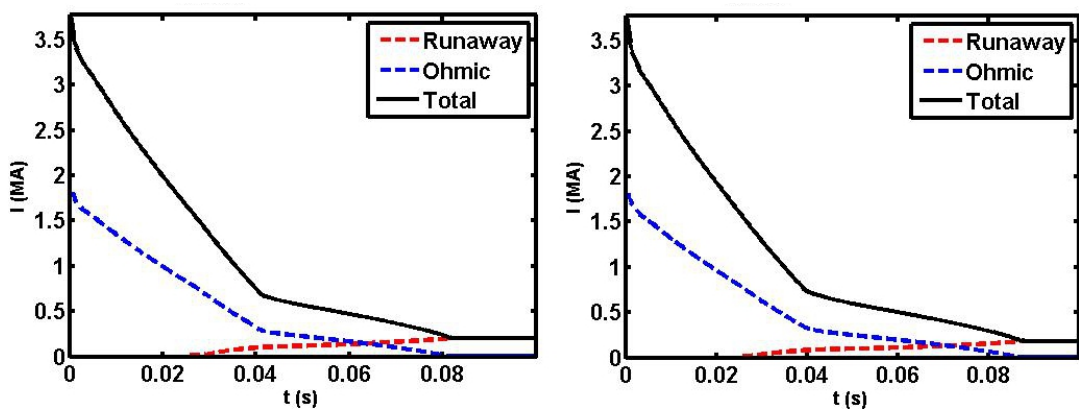
Figure 4.16: Discharge #81928, $n_{Ar}/n_e = 0.2$. Plasma current (left) $n_{Be}/n_e = 0$,(right) $n_{Ar}/n_e = 0.05$.

	Argon 20%	Argon 50%
Beryllium 0%	0.203	0.9686
Beryllium 5%	0.179	0.9646
Beryllium 10%	0.163	0.9641

Table 4.3: Discharge #81928 - Runaway current (in MA) production for different Ar+Be mixtures

4.2.6 Generation mechanisms and the influence of impurities

As runaways are generated by different mechanisms, the impact on runaway production from the main two contributions (primary and secondary generation) of different impurity levels could be investigated. In particular, the aim is to evaluate the fraction of the total runaways coming from the Dreicer mechanism over the total runaways for pure argon and different mixtures of carbon/beryllium plus argon, for both the ILW and carbon wall discharges. In such a way, it is possible to focus on the ratio between Dreicer and avalanche generated runaways, avoiding the problem of the different current evolution due to slight differences in the initial condition of the plasma discharge. For discharge #79423 where a carbon wall is present, the results obtained for different values of argon adjusted to amount of carbon impurities (as a parameter), are in general in agreement with the Dreicer current generated in presence of pure argon. This trend indicates (Fig.4.17) that carbon impurities do not have a strong effect on the fraction of RE generated by the Dreicer mechanism.

When beryllium is injected, the same analysis of the relation between argon level and percentage of impurities, leads to different conclusions for the #81928 discharge. While at low argon concentration (10%) the fraction of Dreicer current is still preponderant, turning to a value of 20% for argon impurities, the situation suddenly changes: a drop in the ratio of REs generated by differen mechanisms occurs, showing an extreme change from 90% of Dreicer-generated REs, to less than 40% or lower for all the beryllium impurities in the scanned range. Increasing more the argon percentage further, a slow recovery of the Dreicer percentage is seen, approaching the Dreicer fraction found in the pure argon case. Therefore

the gap between the pure argon scenario and the 20% beryllium impurity level, confirms both the presence of lower runaway currents and Dreicer currents in the ILW scenario.
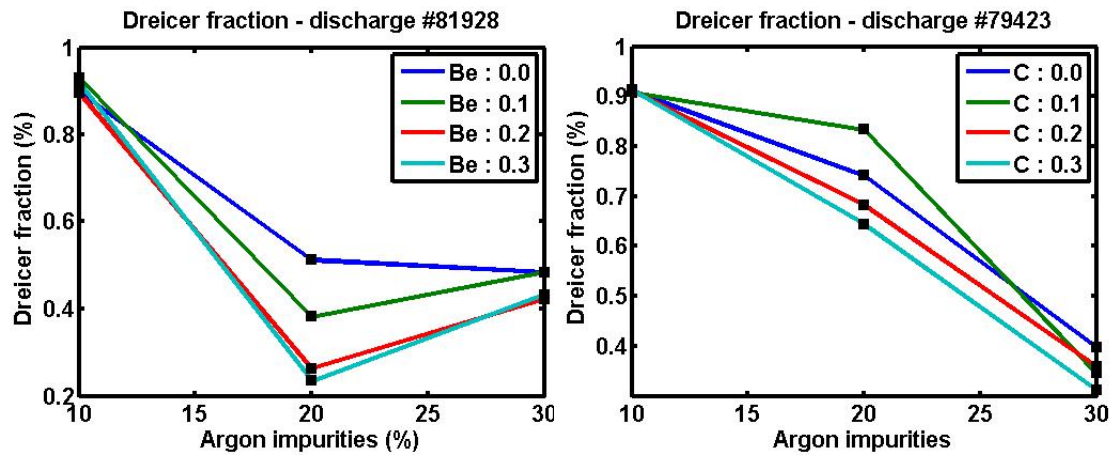
Figure 4.17: Dreicer currents share of total runaway current in discharge #81928 (left) and discharge #79423 (right)

Chapter 5

Conclusions

Reliability, performance and safety are key requirements for tokamak devices and the occurrence of disruptive phenomena poses serious problems in all these areas. Disruptin mitigation is thus one of the most crucial problems in tokamak-type fusion devices.

During a disruption a sudden loss of magnetic confinement occurs and the energy stored in the plasma is released to the surrounding structures. Electromagnetic effects can lead to large forces exerted on the tokamak vessel and induce currents that can cause serious damage to both the vessel and the whole tokamak structure. The rise in temperature during a disruption can also cause thermal effects on the machine, leading to the sputtering and melting of the first wall materials that can release impurities inside the vacuum chamber. As an effect of the augmented level of impurity, the plasma cools down, resulting in the dramatic rise of the toroidal electric field. If the field exceeds a cricital value, some of the electrons (called runaway electrons) are accelerated continuosly and such beams can cause severe damage to crucial parts of the machine. Understanding the generation mechanisms and the evolution of the runaway electrons is therefore fundamental to predict the effects on the plasma facing components.

In the first chapter of the thesis a general perspective of the energy scenario and the need for an abundant, safe and environment-friendly energy source was discussed. The second chapter presented the main features of confined plasma physics. In particular, the fundamentals of nuclear reactions, plasmas and the

technological solution adopted to solve the problem of the confinement of this extremely hot matter was presented. Also the role of current and future tokamak devices in the fusion programme was pointed out. The crucial concept of collision of charged particles in plasmas was introduced and a mathematical model, together with assumptions and limitations, was eventually presented.

The third chapter went into more detail about the disruption phenomenon introducing the most common plasma instabilities, their cause and the effects that they have on the development of a disruption. Moreover, the different stages of a disruption were described, highlighting the effects on the plasma. Also techniques for avoiding disruptions or softening the effects of the disruptions on the machine were discussed. Finally, runaway electron theory was presented, discussing the effects of collision as a friction force opposing the rise of runaway electrons and introducing the concept of critical field. Both primary and secondary runaway electron generation mechanisms as well as loss mechanisms were discussed.

The last chapter was aimed at modeling the runaway generation in presence of impurities, by considering both the evolution of the runaway current and the electric field diffusion in the plasma using the GO code. The analysis focused on the effect of temperature evolution and impurity levels on runaway electron current evolution, pointing out the role of beryllium impurities due to the installation of the *ITER-like wall (ILW)* in JET. Experimental data taken from two *JET* discharges equipped with different walls (carbon and beryllium) were processed to perform the simulations.

First, an exponential decay of plasma temperature was considered and the effects of the final temperature on the runaway currents were investigated. Simulations confirmed that higher final temperatures, in the exponential decay scenario, generates lower runaway currents. A second set of simulations was carried out in a different scenario involving the injection of argon, both pure and mixed with beryllium and carbon. Effects due to differences in the rate of injection were recognized, highlighting that a faster argon injection leads to an increase in the generated runaway current. Several scans for the quantity of argon injected have also been carried out and the simulations showed, as a general trend for both wall

types, that larger amounts of injected argon lead to a faster Ohmic decay and a larger runaway current production.

Finally the role of beryllium and its comparison against the former carbon wall used in *JET* has been evaluated through analyzing a mixed scenario with both argon-carbon and argon-beryllium impurity mixtures. Comparison was also used to assess the magnitude of the primary and secondary generation mechanisms with different impurity amounts, demonstrating that the presence of beryllium is beneficial in case of a reasonable amount of injected argon.

Future works should investigate further features related to the runaway generation, enriching the model with loss mechanisms (e.g. including the effects of magnetic perturbations) and taking also into account the motion of plasma column, that actually occurs during a disruptive phases.

References

[1] I. E. Agency, "Energy balances of OECD countries 2012," v, 2

[2] J. Cramwinckel, "Water and energy nexus–role of technology," *Re-thinking Water and Food Security*, p. 309, 2006. v, 2

[3] R. Goldston, "An indispensable truth: How fusion power can save the planet," *Physics Today*, vol. 65, no. 2, p. 51, 2012. v, 3

[4] British Petroleum, "BP statistical review of world energy," *Yearly rewiew*, 2008. v, 4

[5] G. Papp, "The effect of ITER-like wall on runaway electron generation in JET," *Nuclear Fusion*, submitted for publication. v, vi, 35, 40

[6] B. Areas, "World population," *World Population to 2300*, vol. 236, 2004. 1

[7] O. A. E. A. (IAEA), "Uranium 2011," 2012. 4

[8] W. Han and D. Ward, "Revised assessments of the economics of fusion power," *Fusion Engineering and Design*, vol. 84, no. 2, pp. 895–898, 2009. 5

[9] D. Bednyagin and E. Gnansounou, "Real options valuation of fusion energy R&D programme," *Energy Policy*, vol. 39, no. 1, pp. 116–130, 2011. 5

[10] R. Prince, *Radiation Protection at Light Water Reactors*. Springer Verlag, 2012. 8

[11] J. Lawson, "Some criteria for a power producing thermonuclear reactor," *Proceedings of the Physical Society. Section B*, vol. 70, no. 1, p. 6, 2002. 8

[12] S. Mirnov, "Do spherical tokamaks have a thermonuclear future?," *Plasma physics reports*, vol. 38, no. 12, pp. 931–940, 2012. 9

[13] M. Huguet and D. Smart, "The Joint European Torus - Engineering aspects of the JET nuclear fusion project," *Proceedings of the Institution of Mechanical Engineers*, vol. 193, no. 1, pp. 111–123, 1979. 11

[14] F. Romanelli, J. Paméla, R. Kamendje, M. Watkins, S. Brezinsek, Y. Liang, X. Litaudon, T. Loarer, D. Moreau, D. Mazon, *et al.*, "Recent contribution of JET to the ITER physics," *Fusion Engineering and Design*, vol. 84, no. 2, pp. 150–160, 2009. 11

[15] C. Gormezano *et al.*, "Progress in the ITER physics basis," *Nucl. Fusion*, vol. 47, pp. S285–S336, 2007. 11

[16] U. Fischer, Y. Chen, S. Simakov, P. Wilson, P. Vladimirov, and F. Wasast-jerna, "Overview of recent progress in IFMIF neutronics," *Fusion engineering and design*, vol. 81, no. 8, pp. 1195–1202, 2006. 12

[17] K. Lackner, R. Andreani, D. Campbell, M. Gasparotto, D. Maisonnier, and M. Pick, "Long-term fusion strategy in europe," *Journal of nuclear materials*, vol. 307, pp. 10–20, 2002. 12

[18] H. Pero and S. Paidassi, "The EU fusion programme and roadmap," *Fusion Engineering and Design*, 2012. 12

[19] J. Callen, "Fundamentals of plasma physics," *Madison, USA*, 2003. 13, 15

[20] A. Lightman, *Great ideas in physics: the conservation of energy, the second law of thermodynamics, the theory of relativity, and quantum mechanics.* McGraw-Hill Professional, 2000. 15

[21] J. Wesson, *Tokamaks*, vol. 149. OUP Oxford, 2011. 16, 25, 33, 66

[22] A. Cardella, H. Gorenflo, A. Lodato, K. Ioki, and R. Raffray, "Effects of plasma disruption events on ITER first wall materials," *Journal of nuclear materials*, vol. 283, pp. 1105–1110, 2000. 18

[23] J. Goedbloed and S. Poedts, *Principles of magnetohydrodynamics: With applications to laboratory and astrophysical plasmas.* Cambridge Univ Pr, 2004. 19

[24] G. Neilson, A. Reiman, M. Zarnstorff, A. Brooks, G. Fu, R. Goldston, L. Ku, Z. Lin, R. Majeski, D. Monticello, *et al.*, "Physics issues in the design of high-beta, low-aspect-ratio stellarator experiments," *Physics of Plasmas*, vol. 7, p. 1911, 2000. 20

[25] H. Zohm, M. Maraschek, G. Pautasso, M. Schittenhelm, S. Sesnic, M. Sokoll, W. Suttrop, M. Alexander, M. Bessenrodt-Weberpals, A. Boozer, *et al.*, "MHD stability and disruption physics in ASDEX upgrade," *Plasma Physics and Controlled Fusion*, vol. 37, p. A313, 1995. 20

[26] F. Wagner, "A quarter-century of H-mode studies," *Plasma Physics and Controlled Fusion*, vol. 49, no. 12B, p. B1, 2007. 20

[27] C. Fiore, P. Bonoli, D. Ernst, M. Greenwald, E. Marmar, M. Redi, J. Rice, S. Wukitch, and K. Zhurovich, "Internal transport barrier production and control in Alcator C-Mod," *Plasma physics and controlled fusion*, vol. 46, no. 12B, p. B281, 2004. 21

[28] R. Yoshino, D. Campbell, E. Fredrickson, N. Fujisawa, R. Granetz, O. Gruber, T. Hender, D. Humphreys, N. Ivanov, S. Jardin, *et al.*, "Characterization of disruption phenomenology in ITER," in *these Proceedings*, 1998. 21

[29] G. Pautasso *et al.*, "Causes, precursors and mechanisms of disruptions in ASDEX Upgrade," in *Proc. Intl. Conf. EPS, Wien*, 1997. 21

[30] V. Riccardo, A. Loarte, *et al.*, "Timescale and magnitude of plasma thermal energy loss before and during disruptions in JET," *Nuclear fusion*, vol. 45, no. 11, p. 1427, 2005. 22

[31] A. Loarte, P. Andrew, G. Matthews, J. Paley, V. Riccardo, T. Eich, C. Fuchs, O. Gruber, A. Herrmann, G. Pautasso, *et al.*, "Expected energy fluxes onto iter plasma facing components during disruption thermal quenches from

multi-machine data comparisons," in *Proc. 20th IAEA Fusion Energy Conf. on Fusion Energy 2004 (Vilamoura, 2004)*, 2004. 22

[32] G. Federici, "Plasma wall interactions in iter," *Physica Scripta*, vol. 2006, no. T124, p. 1, 2006. 22

[33] L. Spitzer Jr and R. Härm, "Transport phenomena in a completely ionized gas," *Physical Review*, vol. 89, no. 5, p. 977, 1953. 22

[34] H. Koslowski, "Operational limits and limiting instabilities in tokamak machines," *Fusion science and technology*, vol. 45, pp. 115–122, 2004. 23

[35] B. Esposito, G. Granucci, P. Smeulders, S. Nowak, J. Martín-Solís, and L. Gabellieri, "Disruption avoidance in the frascati tokamak upgrade by means of magnetohydrodynamic mode stabilization using electron-cyclotron-resonance heating," *Physical review letters*, vol. 100, no. 4, p. 45006, 2008. 23

[36] B. Esposito, G. Granucci, M. Maraschek, S. Nowak, A. Gude, V. Igochine, E. Lazzaro, R. McDermott, E. Poli, J. Stober, *et al.*, "Avoidance of disruptions at high β in ASDEX upgrade with off-axis ECRH," *Nuclear Fusion*, vol. 51, p. 083051, 2011. 23

[37] V. Riccardo *et al.*, "Disruptions and disruption mitigation," *Plasma physics and controlled fusion*, vol. 45, no. 12A, p. A269, 2003. 24

[38] M. Lehnen, A. Alonso, G. Arnoux, N. Baumgarten, S. Bozhenkov, S. Brezinsek, M. Brix, T. Eich, S. Gerasimov, A. Huber, *et al.*, "Disruption mitigation by massive gas injection in JET," *Nuclear Fusion*, vol. 51, no. 12, p. 123010, 2011. 24

[39] J. Martin-Solis, R. Sanchez, and B. Esposito, "Predictions on runaway current and energy during disruptions in tokamak plasmas," *Physics of Plasmas*, vol. 7, p. 3369, 2000. 25

[40] S. Chandrasekhar, "Dynamical friction. i. general considerations: the coefficient of dynamical friction," *Astrophysical Journal*, vol. 97, pp. 255–262, 1943. 25

[41] K. Gál, T. Fehér, H. Smith, T. Fülöp, and P. Helander, "Runaway electron generation during plasma shutdown by killer pellet injection," *Plasma Physics and Controlled Fusion*, vol. 50, no. 5, p. 055006, 2008. 27

[42] P. Parks, M. Rosenbluth, and S. Putvinski, "Avalanche runaway growth rate from a momentum-space orbit analysis," *Physics of Plasmas*, vol. 6, p. 2523, 1999. 28

[43] M. Rosenbluth and S. Putvinski, "Theory for avalanche of runaway electrons in tokamaks," *Nuclear Fusion*, vol. 37, no. 10, p. 1355, 2002. 28, 31

[44] G. Papp, M. Drevlak, T. Fülöp, and P. Helander, "Runaway electron drift orbits in magnetostatic perturbed fields," *Nuclear Fusion*, vol. 51, no. 4, p. 043004, 2011. 28

[45] M. De Rover, A. Schilham, A. Montvai, and N. Cardozo, "Test particle transport in perturbed magnetic fields in tokamaks," *Physics of Plasmas*, vol. 6, p. 2443, 1999. 30

[46] R. Jaspers, N. Cardozo, K. Finken, B. Schokker, G. Mank, G. Fuchs, and F. Schüller, "Islands of runaway electrons in the TEXTOR tokamak and relation to transport in a stochastic field," *Physical review letters*, vol. 72, no. 26, pp. 4093–4096, 1994. 30

[47] T. Evans, R. Moyer, and P. Monat, "Modeling of stochastic magnetic flux loss from the edge of a poloidally diverted tokamak," *Physics of Plasmas*, vol. 9, p. 4957, 2002. 30

[48] A. Rechester and M. Rosenbluth, "Electron heat transport in a tokamak with destroyed magnetic surfaces," *Physical Review Letters*, vol. 40, no. 1, pp. 38–41, 1978. 31

[49] A. Boozer and R. White, "Particle diffusion in tokamaks with partially destroyed magnetic surfaces," *Physical Review Letters*, vol. 49, no. 11, pp. 786–789, 1982. 31

[50] P. Helander, L. Eriksson, and F. Andersson, "Suppression of runaway electron avalanches by radial diffusion," *Physics of Plasmas*, vol. 7, p. 4106, 2000. 31

[51] V. Shafranov, *Reviews of Plasma Physics*, vol. 22. Springer, 2001. 31

[52] T. Fehér, H. Smith, T. Fülöp, and K. Gál, "Simulation of runaway electron generation during plasma shutdown by impurity injection in ITER," *Plasma Physics and Controlled Fusion*, vol. 53, no. 3, p. 035014, 2011. 33, 34

[53] L.-G. Eriksson, P. Helander, F. Andersson, D. Anderson, and M. Lisak, "Current dynamics during disruptions in large tokamaks," *Physical review letters*, vol. 92, no. 20, p. 205004, 2004. 34

[54] A. Quarteroni and A. Valli, *Numerical approximation of partial differential equations*, vol. 23. Springer, 2008. 34

[55] A. Quarteroni, R. Sacco, and F. Saleri, *Numerical mathematics*, vol. 37. Springer, 2006. 34

[56] P. de Vries, G. Arnoux, A. Huber, J. Flanagan, M. Lehnen, V. Riccardo, C. Reux, S. Jachmich, C. Lowry, G. Calabro, *et al.*, "The impact of the ITER-like wall at JET on disruptions," *Plasma Physics and Controlled Fusion*, vol. 54, no. 12, 2012. 35

[57] V. Izzo, E. Hollmann, A. James, J. Yu, D. Humphreys, L. Lao, P. Parks, P. Sieck, J. Wesley, R. Granetz, *et al.*, "Runaway electron confinement modelling for rapid shutdown scenarios in DIII-D, alcator C-Mod and ITER," *Nuclear Fusion*, vol. 51, no. 6, p. 063032, 2011. 42

[58] P. Helander and D. Sigmar, *Collisional transport in magnetized plasmas*, vol. 87. Cambridge University Press, 2002. 65, 66

[59] C. Villani, "Conservative forms of Boltzmann's collision operator: Landau revisited," *ESAIM: Mathematical Modelling and Numerical Analysis*, vol. 33, no. 01, pp. 209–227, 1999. 65

[60] S. I. Braginskii, "The concept of indistinguishable particles in classical and quantum physics," *Reviews of Plasma Physics*, vol. 1, 1957. 66

[61] R. Alexandre and C. Villani, "On the Landau approximation in plasma physics," in *Annales de l'Institut Henri Poincare (C) Non Linear Analysis*, vol. 21, pp. 61–95, Elsevier, 2004. 66

[62] H. Risken, *The Fokker-Planck equation: Methods of solution and applications*, vol. 18. Springer Verlag, 1996. 66

Appendix A

This appendix holds the main parameters of the simulations used in this work.

The list includes discharge type (#79423 or #81928), amount of gas injected (if present) and injection time constant (in *ExpDecay* scenario, the injection time constant does not apply, and instead it is to be considered as referring to the decay constant.) Gas injection for each species s (argon, carbon and beryllium) is expressed as fraction α of the initial electron density $n_e(r, t = 0)$:

$$\alpha = n_s(r, t = t_{sat})/n_e(r, t = 0), \tag{1}$$

where t_{sat} is the saturation value for the injection as shown in Fig.4.6. The column discharge refers not only to the discharge for which the simulation has been carried out, but also define different profiles for temperature and density used for sensitivity analysis with respect to initial parameters.

Discharge	T (eV)	n (atoms $\cdot m^{-3}$)
JET 81928Be	$2.45555 \cdot 10^3 (1 - 0.982376 \cdot x^2)^2$	$3.17109 \cdot 10^{19} (1 - 1.2228 \cdot x^2)^2$
81928	$1486 \cdot (1 - 0.982376 \cdot x^2)^2$	$3.17109 \cdot 10^{19} (1 - 1.3228 \cdot x^2)^2$
JET Carbon wall	$2.17494 \cdot 10^3 (1 - 1.0319 \cdot x^2)^2$	$19(1 - 1.27186 \cdot x^2)^{0.42733}$
JET 74923	$3.1001 \cdot 10^3 (1 - 0.9 \cdot x^2)^2$	$2.8 \cdot 10^{19} (1 - 0.9 \cdot x^2)^{0.6623}$

Table 1: Profiles used in the simulations

Discharge	Inj. time(s)	Sim. time (ms)	Scenario	Ar	C	Be
JET 81928Be	0.00030	8	ExpDecay	0.00	0.00	0.00
81928	0.00001	110	GasInject	0.10	0.00	0.00
81928	0.00001	1	GasInject	0.10	0.00	0.00
81928	0.00010	110	GasInject	0.10	0.00	0.00
81928	0.00100	110	GasInject	0.10	0.00	0.00
81928	0.00001	110	GasInject	0.10	0.00	0.00
81928	0.01000	110	GasInject	0.10	0.00	0.00
81928	0.00030	500	GasInject	0.30	0.00	0.00
81928	0.00030	50	GasInject	0.10	0.00	0.00
81928	0.00001	110	GasInject	0.10	0.00	0.00
81928	0.00001	110	GasInject	0.30	0.00	0.00
81928	0.00001	110	GasInject	0.10	0.00	0.00
81928	0.00001	110	GasInject	0.50	0.00	0.00
81928	0.00001	110	GasInject	0.10	0.00	0.00
81928	0.00001	110	GasInject	0.10	0.00	0.00
JET 81928Be	0.00001	15	GasInject	0.10	0.00	0.00
JET 81928Be	0.10000	55	GasInject	0.20	0.00	0.00
JET 81928Be	0.00030	70	GasInject	0.10	0.00	0.00
JET 81928Be	0.00030	70	GasInject	0.50	0.00	0.00
JET carbon wall	0.00030	600	ExpDecay	0.00	0.00	0.00
JET carbon wall	0.00030	600	ExpDecay	0.00	0.00	0.00
JET carbon wall	0.00030	600	ExpDecay	0.00	0.00	0.00
JET carbon wall	0.00030	600	ExpDecay	0.00	0.00	0.00
JET carbon wall	0.00030	600	ExpDecay	0.00	0.00	0.00
JET carbon wall	0.00001	110	GasInject	0.10	0.00	0.00
JET carbon wall	0.00001	110	GasInject	0.10	0.00	0.00
JET carbon wall	0.00001	110	GasInject	0.10	0.00	0.00
JET carbon wall	0.00001	110	GasInject	0.30	0.00	0.00
JET carbon wall	0.00001	110	GasInject	0.20	0.00	0.00
JET carbon wall	0.00001	110	GasInject	0.50	0.00	0.00
JET carbon wall	0.00001	110	GasInject	0.30	0.00	0.00
JET carbon wall	0.00001	150	GasInject	0.10	0.00	0.00
JET carbon wall	0.00010	110	GasInject	0.10	0.00	0.00
JET carbon wall	0.00030	110	GasInject	0.30	0.00	0.00
JET carbon wall	0.00100	110	GasInject	0.10	0.00	0.00
JET carbon wall	0.00030	110	GasInject	0.50	0.00	0.00
JET carbon wall	0.00316	110	GasInject	0.10	0.00	0.00

Discharge	Inj. time(s)	Sim. time (ms)	Scenario	Ar	C	Be
JET carbon wall	0.01000	110	GasInject	0.10	0.00	0.00
JET carbon wall	0.00030	1	GasInject	0.10	0.00	0.00
JET carbon wall	0.00001	110	GasInject	0.10	0.00	0.00
JET carbon wall	0.00001	110	GasInject	0.10	0.00	0.00
JET carbon wall	0.00001	110	GasInject	0.10	0.00	0.00
JET carbon wall	0.00001	110	GasInject	0.10	0.00	0.00
JET carbon wall	0.00001	110	GasInject	0.10	0.00	0.00
81928	0.00030	1000	GasInject	0.20	0.00	0.10
81928	0.00030	100	GasInject	0.00	0.00	0.30
81928	0.00030	100	GasInject	0.50	0.00	0.05
81928	0.00030	100	GasInject	0.50	0.00	0.10
81928	0.00030	100	GasInject	0.20	0.00	0.10
81928	0.00030	100	GasInject	0.20	0.00	0.00
81928	0.00030	100	GasInject	0.10	0.00	0.00
81928	0.00030	100	GasInject	0.49	0.00	0.00
81928	0.00030	100	GasInject	0.30	0.00	0.00
81928	0.00030	100	GasInject	0.20	0.00	0.00
81928	0.00030	100	GasInject	0.20	0.00	0.05
81928	0.00030	100	GasInject	-0.00	0.00	0.10
81928	0.00030	100	GasInject	0.20	0.00	0.05
81928	0.00030	100	GasInject	0.49	0.00	0.05
81928	0.00030	100	GasInject	0.20	0.00	0.10
81928	0.00030	100	GasInject	-0.00	0.00	0.20
81928	0.00030	100	GasInject	0.49	0.00	0.10
81928	0.00030	110	GasInject	0.20	0.00	0.30
81928	0.00030	50	GasInject	0.20	0.00	0.20
81928	0.00030	50	GasInject	0.10	0.00	0.20
81928	0.00030	50	GasInject	0.30	0.00	0.30
81928	0.00030	50	GasInject	0.10	0.00	0.30
81928	0.00030	50	GasInject	0.10	0.00	0.10
81928	0.00030	50	GasInject	0.30	0.00	0.10
81928	0.00030	50	GasInject	0.30	0.00	0.20
81928	0.00030	50	GasInject	0.20	0.00	0.10
81928	0.00030	50	GasInject	0.30	0.00	0.20
81928	0.00030	50	GasInject	0.30	0.00	0.30
81928	0.00030	50	GasInject	0.20	0.00	0.30
81928	0.00001	55	GasInject	0.00	0.00	0.10
81928	0.00030	100	GasInject	0.50	0.00	0.10
JET 79423	0.00030	100	GasInject	0.50	0.10	0.00
JET 79423	0.00030	100	GasInject	0.30	0.10	0.00

Discharge	Inj. time(s)	Sim. time (ms)	Scenario	Ar	C	Be
JET 79423	0.00030	100	GasInject	0.30	0.30	0.00
JET 79423	0.00030	100	GasInject	0.10	0.10	0.00
JET 79423	0.00030	100	GasInject	0.10	0.20	0.00
JET 79423	0.00030	100	GasInject	0.10	0.29	0.00
JET 79423	0.00030	100	GasInject	0.50	0.00	0.00
JET 79423	0.00030	100	GasInject	0.20	0.05	0.00
JET 79423	0.00030	100	GasInject	0.10	0.29	0.00
JET 79423	0.00030	100	GasInject	0.50	0.00	0.00
JET 79423	0.00030	100	GasInject	0.20	0.00	0.00
JET 79423	0.00030	100	GasInject	0.50	0.05	0.00
JET 79423	0.00030	100	GasInject	0.20	0.20	0.00
JET 79423	0.00030	100	GasInject	0.20	0.10	0.00
JET 79423	0.00030	100	GasInject	0.20	0.29	0.00
JET 79423	0.00030	100	GasInject	0.10	0.00	0.00
JET 79423	0.00030	100	GasInject	0.20	0.00	0.00
JET 79423	0.00030	100	GasInject	0.30	0.00	0.00
JET 79423	0.00030	100	GasInject	0.30	0.10	0.00
JET 79423	0.00030	100	GasInject	0.30	0.20	0.00
JET carbon wall	0.00030	100	GasInject	0.10	0.20	0.00
JET carbon wall	0.00001	25	GasInject	0.00	0.30	0.00
JET carbon wall	0.00001	25	GasInject	0.00	0.30	0.00
JET carbon wall	0.00001	25	GasInject	0.00	0.10	0.00
JET carbon wall	0.00001	25	GasInject	0.00	0.20	0.00
JET carbon wall	0.00001	25	GasInject	0.00	0.20	0.00
JET carbon wall	0.00001	25	GasInject	0.00	0.30	0.00
81928	0.00010	110	GasInject	0.10	0.00	0.00
81928	0.00100	110	GasInject	0.10	0.00	0.00
81928	0.00001	110	GasInject	0.10	0.00	0.00
81928	0.01000	110	GasInject	0.10	0.00	0.00
JET carbon wall	0.00001	110	GasInject	0.10	0.00	0.00
JET carbon wall	0.00010	110	GasInject	0.10	0.00	0.00
JET carbon wall	0.00316	110	GasInject	0.10	0.00	0.00
JET carbon wall	0.01000	110	GasInject	0.10	0.00	0.00

Appendix B

A suitable collision operator must consider all the collisions among different kinds of particles. In the general form, let a be the scatteree particle and b the scattered particle, the collision operator can be written as:

$$\mathcal{C}^{ab}(f_a, f_b) = -\frac{\partial}{\partial \mathbf{v}} \cdot (\mathbf{A}^{ab} f_a) + \frac{\partial^2}{\partial \mathbf{v} \partial \mathbf{v}} : \mathbf{D}^{ab} f_a, \tag{2}$$

where $\mathbf{A}$ and $\mathbf{D}$ are respectively the *friction coefficient* and the *diffusion coefficient*. The exact expressions for these coefficients reads [58]:

$$\mathbf{A}^{ab} = -\Gamma^{ab} \left(1 + \frac{m_a}{m_b}\right) \int d^3\mathbf{w} f_b(w) \frac{\mathbf{v} - \mathbf{w}}{|\mathbf{v} - \mathbf{w}|^3}, \tag{3}$$

$$\mathbf{D}^{ab} = \frac{1}{2}\Gamma^{ab} \int d^3\mathbf{w} f_b(w) \frac{1}{|\mathbf{v} - \mathbf{w}|} \left(\mathbf{I} - \frac{(\mathbf{v} - \mathbf{w})(\mathbf{v} - \mathbf{w})}{|\mathbf{v} - \mathbf{w}|^2}\right), \tag{4}$$

where the term Γ^{ab} absorbs all the constants present in the kinetic equations:

$$\Gamma^{ab} = \frac{4\pi Z_a^2 Z_b^2 e^4 \ln \Lambda}{m_a^2}. \tag{5}$$

Using such a model eventually leads, after algebraic and calculus manipulations [59], to an equivalent form for the collision operator, known as the *Landau form* of the Fokker-Planck operator:

$$\mathcal{C}^{ab}(f_a, f_b) = \frac{1}{2}\Gamma^{ab} \frac{\partial}{\partial \mathbf{v}} \int d^3\mathbf{w} \mathbf{U}(\mathbf{v}, \mathbf{w}) \cdot \left(\frac{\partial}{\partial \mathbf{v}} - \frac{m_a}{m_b} \frac{\partial}{\partial \mathbf{w}}\right) f_b(\mathbf{w}) f_a(\mathbf{v}), \tag{6}$$

where $\mathbf{u} = \mathbf{v} - \mathbf{w}$, $u = |\mathbf{u}|$ and the term $\mathbf{U}(\mathbf{v}, \mathbf{w}) = \frac{1}{u}\left(\mathbf{I} - \frac{\mathbf{u}\mathbf{u}}{u^2}\right)$ is the *scattering tensor* [60]. Adopting the approximation $m_e/m_i \to 0$ [61], the first term in (6) dominates and the ion distribution acts like a delta function $f_i(\mathbf{w}) \approx n_i\delta(\mathbf{w})$ compared to the electron velocity scale. This results from electrons scattering off ions, producing mainly an effect of angular deflection and lower order effects for energy exchange[1]. The effect of such assumptions on the Landau operator is to make it completely linear and by choosing a spherical coordinate system, it is possible [62] [58] to get:

$$\frac{\partial}{\mathbf{v}} \cdot \frac{1}{v}\left(\mathbf{I} - \frac{\mathbf{v}\mathbf{v}}{v^2}\right) \cdot \frac{\partial}{\mathbf{v}} = \frac{1}{v^3}2\mathfrak{L}, \tag{7}$$

where $2\mathfrak{L}$ is the the angular part of the Laplacian operator and is called *Lorentz scattering operator*. A further assumption that leads to the ultimate form for the collisional operator and that is suitable for a fusion plasma, is to consider one of the two species (e.g. b) to be Maxwell-distributed and at rest[2]. The rate of deceleration of a species a particle due to the impact on a species b particle (called *slowing down frequency* ν_s^{ab}) is to be considered together with the *deflection frequency* ν_D^{ab} associated to the rate of change in the direction of the velocity vector. Also a frequency term for *parallel velocity diffusion* $\nu_{\parallel}$ has to be considered. The collision operator is therefore simplified:

$$\mathcal{C}^{ab}(f_a, f_b) = \nu_{defl}^{ab}\mathfrak{L}(f_a) + \frac{1}{\mathbf{v}^2}\frac{\partial}{\partial\mathbf{v}}\left[v^3\left(\frac{m_a}{m_a + m_b}\nu_{slow}^{ab}f_a + \frac{\nu_{diff}^{ab}\mathbf{v}}{2}\frac{\partial f_a}{\partial\mathbf{v}}\right)\right] \tag{8}$$

and the expressions for ν_{slow}^{ab}, ν_{defl}^{ab}, ν_{diff}^{ab} can be found in [21].

---

[1]This scheme is the so-called *Lorentz collision model*, where the ions are supposed to be immobile in the background.

[2]In the case of electrons and ions, just remember the assumption $m_i \to \infty$ and the consequent small scale effects on energy exchanges in ion-electron collision.